



PHYSICS DEPARTMENT, PRINCETON UNIVERSITY

The DarkSide-LowMass Experiment and its Physics Potential

Junior Paper

This paper represents my own work in accordance with University regulations.
/s/Gabriele Montefalcone

Undergraduate Student:
Gabriele Montefalcone

Advisor:
Prof. Cristiano Galbiati

Researchers:
PostDoc. Claudio Savarese
PostDoc. Masayuki Wada

Abstract

The concept of dark matter was developed several decades ago to explain the anomalous motions of galaxies gravitationally bound in clusters. Since then, observational evidence has accumulated, and dark matter is now a widely accepted concept around the scientific community. Indeed, the existence of a form of matter that is “dark” and thus only interacts through its gravitational effects, explains naturally many cosmological puzzles such as the structure and distribution of galaxies and their clusters, the fluctuations in the cosmic microwave background radiation and the rate of expansion of the universe. Today, its nature still remains unknown.

Among all the possible species of dark matter, the Weakly Interacting Massive Particles (WIMPs) form a class of candidates capable of explaining this physics puzzle in a natural way. Many experiments aim for a WIMP direct detection under the leading assumption that dark matter can, even if very rarely, interact with particles from the Standard Model. The rarity of such interactions makes them very challenging to detect. Any background can mask the signal they produce, and its rejection is therefore the major problem in dark matter detection.

Most models predict dark matter WIMP masses near the electroweak scale of 100’s of GeV/c^2 . However, dark matter particle masses $\leq 10 \text{ GeV}/c^2$ can also be compatible with experimental constraints if a significant asymmetry between dark matter and their anti-particles existed in the early Universe.

In 2018, the DarkSide Collaboration, one of the strongest experimental projects in the direct search for DM, achieved the world-leading limits for *low-mass* DM with nucleon scattering cross section between 10^{-41} to 10^{-42} cm^2 . This was accomplished by a blind analysis of the 532.4-live-day data set from the DarkSide-50 experiment, a dual-phase argon time projection chamber nested within a system of active vetoes, the inner for neutron tagging and the outer for muon rejection, operating at LNGS (Italy).

The experimental sensitivity of DarkSide-50, in this WIMP mass range, is limited by the electron recoil background from the detector materials (mainly the photomultiplier tubes (PMTs), the cryostat, and the radioactive noble gases residual in the argon target). To ensure a complete exploration of this region of the WIMP parameter space there needs a further improvement in sensitivity by more than two orders of magnitude. Such an ambitious goal requires larger target exposures and a lower background.

In this research, I compare different solutions for the detector, including the geometry and materials used, to demonstrate the feasibility of a DarkSide-LowMass experiment with the highest achievable sensitivity at the current state of the technology.

To do so, I will run several MonteCarlo simulations using a modified version of GEANT-4 based G4DS MonteCarlo package and produce the expected background and the sensitivity projections for both a standard DS-50 like detector and the proposed DS-LowMass detector.

In Chapter 1 I introduce dark matter, its evidence and the physics of the DarkSide detectors.

In Chapter 2 I describe the geometry, functioning and the various background sources of the two detectors I will consider in this paper.

In Chapter 3 I explain the method used to simulate the experiment and to analyze the data obtained.

Finally, in Chapter 4 I will show the results collected and discuss their implications.

Contents

1	Introduction to Dark Matter	1
1.1	Evidence of Dark Matter	1
1.1.1	Galactic rotation curves	1
1.1.2	Gravitational Lensing	2
1.1.3	The Cosmic Microwave Background (CMB)	3
1.2	Dark Matter Candidates	4
1.2.1	Neutrinos	5
1.2.2	Axions	6
1.2.3	WIMPs	6
1.3	WIMPs Detection Techniques	8
1.3.1	WIMP search through production	8
1.3.2	WIMP indirect search	8
1.3.3	WIMP direct search	8
1.4	The DarkSide Program	9
2	The Dark-Side LowMass Detector	13
2.1	The DS-Proto Detector	13
2.2	The DS-LowMass Detector	16
2.3	Sources of Background	18
2.3.1	Cosmogenic Muons	18
2.3.2	β -Decays	19
2.3.3	α -Decays	19
2.3.4	γ -Rays and X-Rays	19
2.3.5	Neutrons	19
2.4	Relevant background-producing Radioisotopes	20
2.4.1	^{39}Ar	20
2.4.2	^{60}Co	20
2.4.3	^{40}K	21
2.4.4	^{232}Th	21
2.4.5	^{238}U	21
2.4.6	^{235}U	21

3	Simulations and Analysis	22
3.1	MonteCarlo (MC) Simulations	22
3.1.1	G4DS: The MC Package for the DarkSide Program	22
3.1.2	MC Simulations Generated	23
3.2	The Analysis Process	25
3.2.1	From MC Simulations to Observables	25
3.2.2	Selection Cuts	26
3.2.3	Normalization	27
4	Results and Limit Calculation	31
4.1	The standard DS-Proto Detector	31
4.2	The New DS-LowMass Detector	32
4.3	Limit Calculation	33
4.4	Conclusions	35
A	SiPMs components Activities	36

List of Figures

1.1	Rotation curve of NGC 6503	2
1.2	Gravitational Lensing of Abell 2218 cluster	3
1.3	The Cosmic Microwave Background	4
1.4	Evolution of the WIMP number density	7
1.5	The DarkSide 50 detector	10
1.6	C.L. exclusion curve from DarkSide 50	11
2.1	SQB and TRBs assemblies of tiles	14
2.2	Field cage and Reflector panels of the LAr TPC	15
2.3	DarkSide-Proto LAr TPC	15
2.4	DarkSide-Proto Cryostat	16
2.5	The Liquid Scintillator Neutron Veto	17
2.6	The DarkSide LowMass Detector	18
3.1	Conversion Curve from electron recoil spectra to ionization spectra	25
3.2	Selection Cuts applied to the N_{e^-} background spectrum in the SiPMs	27
4.1	N_{e^-} background spectrum for the DarkSide-Proto detector	32
4.2	N_{e^-} background spectrum for the DarkSide-LowMass detector	33
4.3	The 90 % C.L. projected exclusion curves for DS-Proto and DS-LowMass	34

List of Tables

3.1	List of the number of events simulated per radioisotope in each of the 5 detector components	24
3.2	Total mass of all the materials that compose the detectors	29
3.3	List of the activities of each of the radioisotopes simulated in each of the materials that compose the detectors	29
3.4	List of the total activity of the radioisotopes simulated in all the components of the detector	30
A.1	Mass and units of each component of the SiPMs for the two detectors considered in this research. The elements are divided in two categories: those composing the actual tiles and those making the FEB.	37
A.2	Radioisotopes activity in every SiPM component as found in the DarkSide materials database [1]. As we can clearly observe many data are missing or are only limits on the actual activities which if accurately measured will probably result to be much lower than shown.	38

Chapter 1

Introduction to Dark Matter

1.1 Evidence of Dark Matter

Dark matter refers to the various candidates for non-luminous matter in the universe whose effects have only been observed so far through the gravitational pull it exerts. Its identity and properties are still one of the biggest mysteries in modern physics. While direct detection of dark matter interacting with other forms of matter is lacking, its existence is supported by mounting evidence of its gravitational effects, accumulated over many decades. In particular, three important pieces of evidence come from studies of galactic rotation curves, gravitational lensing and the cosmic microwave background, and are described in detail below.

1.1.1 Galactic rotation curves

A very strong evidence for the existence of dark matter comes from the rotation curves of the galaxies or, in other terms, the circular velocities of stars and gas in a galaxy as a function of the distance from the galactic center. Observations of spiral galaxies indicate that they typically consist of a dense central bulge where is concentrated the vast majority of the mass. Thus, a simple approximation would be to consider all the mass of the galaxy uniformly distributed in this volume. According to Newtonian dynamics, the circular velocity of a galaxy is then given by:

$$v(r) = \sqrt{\frac{GM(r)}{r}}, \quad (1.1)$$

Where $M(r) = \int \rho(r)r^2 dr$ and $\rho(r)$ is the mass density profile of the galaxy. The circular velocity is expected to increase from the center to the edge of the galaxy and then to fall as $\frac{1}{\sqrt{r}}$ beyond the optical disk. However, as can be seen in Figure 1.1, the measured rotation curves do not agree with the predictions of equation 1.1. Indeed, at very large radii, beyond the optical disk, the velocity remains constant instead of decreasing. The same kind of discrepancy is also observed for galaxies rotating in clusters of galaxies.

These phenomena can only be explained in two ways: either we need a modified theory of gravity or the mass of the galaxies is much more than the fraction we observe.

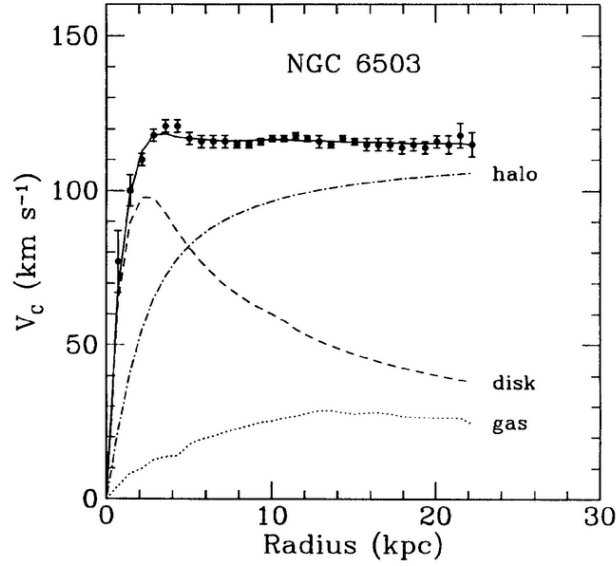


Figure 1.1: Example of rotation curve with a flat behaviour beyond the edge of the optical disk: the data are taken from the galaxy NGC 6503 and are represented in the graph by the bullet points, the dash-dotted line named disk is the rotation curve that we would expect if the mass was all distributed inside the disk. The other dash-dotted line represent the dark matter halo contribution that would be needed to explain the observed rotation curves of NGC 6503. Credit: [2]

This large discrepancy with the predictions of galactic rotation curves can therefore be resolved by postulating the existence of a non-luminous matter in the form of a dark matter halo such that such that $M(r) \propto r$ and $v(r) \approx \text{constant}$ for $r > R$ where R is the radius of the central bulge.

1.1.2 Gravitational Lensing

Another strong piece of evidence for the existence of dark matter comes from the gravitational lensing effects caused by clusters of galaxies. As predicted by Einstein's theory of general relativity, massive objects curve the spacetime around them, so that the path of light can be significantly distorted in strong gravitational fields. As a result, the light emitted by objects behind the cluster can be very deflected such that we will observe small shape distortions or, in some cases, a clear separation into multiple images of the same object, as show in Figure 1.2. The mass of the galaxy cluster can be then inferred by measuring the geometry of the distortion and the deflection angle. The observed lensing effect resulted to be much stronger than what expected by assuming only the contribute of stars and gas in the cluster. Assuming the validity of General Relativity, then galaxies and clusters of galaxies are dominated by some form of non-baryonic matter which would account for 90% of the total effect.

Further evidence of this theory was furnished by the observation of gravitational lensing of the Bullet cluster, a system composed of two clusters that collided in the past. Indeed measurements of gravitational lensing caused by these galaxies can give an indication of the center of mass of all matter. On the other hand, since the mass of these galactic clusters is dominated by interstellar gas and stars, optical techniques such as x-ray photography can provide an independent measure of the

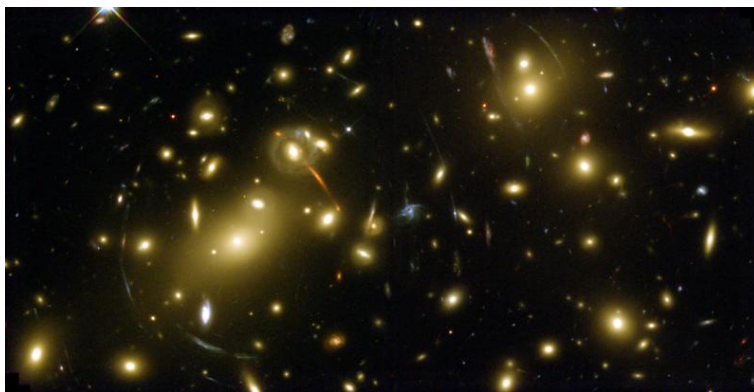


Figure 1.2: Example of strong gravitational lensing of Abell 2218 cluster. Here, the effects of gravitational lensing are observed in the stretching of the distant, lensed galaxies which are pulled into arcs as the light passes close to the foreground cluster. The real galaxies are not this shape, they are usually elliptical or spiral shaped, they just appear this way because of lensing. Credit: [3]

baryonic mass distribution in both galaxies. Surprisingly, the measurements of the center of mass using the two different techniques differed drastically, implying that the center of mass of baryonic matter differ from the total center of mass by over 8σ [4]. This discrepancy can be hardly explained by any modified theory of gravity since the center of the total mass should always correspond to point of maximum curvature. Thus these measurements provide a very strong indication for the presence of a non-baryonic, weakly interacting form of matter that represents the dominant mass component of galaxies and clusters of galaxies.

1.1.3 The Cosmic Microwave Background (CMB)

The Cosmic Microwave Background was predicted in 1948 by Ralph Alpher and Robert Herman and measured, for the first time, in 1964 by 2 scientists from Bell Lab, Arno Penzias and Robert Wilson, who observed a mysterious persistent and isotropic microwave background in their radio-wave antenna receiver. [5]

The CMB represents the thermal radiation leftover from the separation of matter and radiation following the Big Bang. Before that moment, the universe was filled with a hot plasma of charged particles and photons in thermal equilibrium. As the universe expanded, the temperature and energies of the particles decreased and when the energy density of the plasma dropped under the hydrogen ionization energy, protons and electrons combined to form neutral hydrogen atoms. This led to the decoupling of photons from matter, which were finally free to propagate instead of being constantly scattered by electrons and protons in plasma. These relic photons form the CMB as we observe it today. Indeed, the wavelength of these photons increased over time due to the expansion of the universe, into the microwave region with an average temperature equivalent to $\sim 2.7K$. The temperature map of the CMB (Figure 1.3) as determined by the Planck mission is very uniform and presents small spatial temperature anisotropies, whose relative amplitude is in the range of 1 part in 10^5 . [6]

The hotter regions in the CMB map correspond to regions denser of matter at the moment of the photon-decoupling which therefore had a corresponding higher gravitational pull. These fluctuations

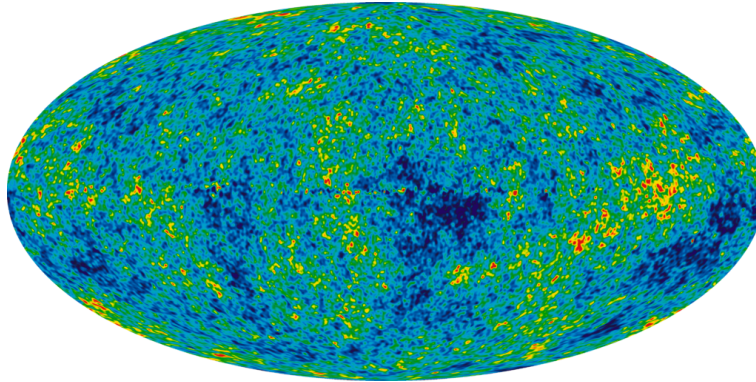


Figure 1.3: The detailed, all-sky picture of the infant universe created from nine years of WMAP data. The image reveals 13.77 billion year old temperature fluctuations (shown as color differences) that correspond to the seeds that grew to become the galaxies. The signal from our galaxy was subtracted using the multi-frequency data. This image shows a temperature range of $\pm 200 \mu\text{K}$. Credit: [7]

are necessary for matter to combine and form more complicated structures. However, given their small intensity, they cannot be considered as the unique seeds of the structure of the cosmos as we observe it today. To solve the problem, we need to introduce a form of electrically neutral matter which interacts only through gravity. Imposing that this form of matter is non-relativistic, it would then enhance the density of the hotter regions, thus accelerating the process of accretion of large structures in the universe.

The study of the distribution and intensity of such anisotropies gave many significant results in cosmology and particle physics. Specifically, an analysis of the CMB power spectrum (plot of the fluctuations in the CMB temperature spectrum at different angular scales) using the ΛCDM cosmology (the “standard model” of Big Bang cosmology) inferred that dark matter accounts for approximately 84% of the total mass of the universe.

1.2 Dark Matter Candidates

The first important categorization for different models is whether dark matter is hot (relativistic), or cold (non-relativistic). As mentioned in section 1.1.3 according to measurements on the CMB, dark matter constitutes 84% of total matter and it was therefore the main driving force in the formation of galactic structure in the early universe. These measurements enable us to reject the possibility of dark matter to be mainly hot because it would not explain the formation of structures in the Universe (galaxies, clusters and larger objects), since these particles would be moving far too quickly to allow the formation of large scale structures. [8]

Another very important concept for understanding the nature of dark matter is the study of the thermal production of elements in the early universe. The expansion and cooling down of the universe determined the development of the production mechanisms of each element and motivate their current abundance. Indeed, at its early stage, the universe was basically in thermal equilibrium, meaning that production and annihilation rates of each particle were approximately the same (this

is true only under the assumption of standard thermal production). [9]

The production mechanism is only efficient for collisions at temperatures $kT > m_\xi c^2$, where m_ξ is the mass of such particle ξ . Indeed if the mean energy per particle in the Universe is smaller than m_ξ , it is impossible to produce many of them and they will generally annihilate or transform into other species.

As the universe expanded, the thermal plasma cooled down and production rates decreased exponentially according to $e^{-\frac{m_\xi c^2}{kT}}$ (the Boltzmann factor) [9]. At the same time, the expansion also diluted the number density n , impacting on the annihilation rate. The key for measuring the relic density of each element is therefore a comparison between the rate of interactions Γ and the rate of expansion H . When the time scale of particle interactions is in the order of the characteristic expansion time scale (eq.1.2) reactions effectively ceased and population of these particles as a whole changed only due to expansion of the space (chemical decoupling) [10].

$$t_\gamma \sim t_h \qquad t_\gamma \equiv \frac{1}{\Gamma} \qquad t_h \equiv \frac{1}{H} \qquad (1.2)$$

The effect of the chemical decoupling is the so-called “freeze-out” [11]. Different particle species may have different interaction rates and so may decouple at different times. Such an analysis is particularly important to estimate many features of a possible dark matter candidate, such as its rest mass and cross section range. These two values m_χ and σ_χ respectively give us information about the amount of energy needed to produce such particles and the probability that a scattering process, due to a given reaction, will occur. What we expect for dark matter is a very large rest mass, roughly heavier than $\sim 1\text{-}100$ keV, and a low cross section, in the order of $\sigma_\chi v \sim 10^{-26} \text{cm}^3/\text{s}$, where v is the relative velocity between the annihilating particles [5]. In this way, dark matter would decouple relatively early on, explaining both its very weakly interaction with ordinary matter and its large abundance in the universe, as predicted by measurements of galactic rotational curves, gravitational lensing and CMB power spectrum.

Here, it follows a brief discussion of the possible DM candidates, whose models are consistent with observations and the just mentioned constrictions.

1.2.1 Neutrinos

When one considers the dark matter problem from the perspective of the standard model of particle physics, the three neutrinos clearly stand out. In fact, unlike all other known particle species, the neutrinos are stable (or at least very long lived) and do not experience electromagnetic or strong interactions. [5] However due to their relativistic nature, they would constitute a hot dark matter candidate which, as mentioned in the previous paragraph, could not account for most of the dark matter in the Universe, leading to very different patterns of large scale structure.

Sterile neutrinos have also been proposed as dark matter candidates. These hypothetical particles are similar to Standard Model neutrinos, but without weak interactions and would only interact, other than through gravity, through a small degree of mixing with the standard model neutrinos.

Depending on their mass, if such sterile neutrinos exist, they could be produced with a wide range of temperatures, and thus could constitute a cold ($m_{\nu_s} \gg \text{keV}$) candidate for dark matter. [5]

1.2.2 Axions

Axions were first introduced by Peccei and Quinn in an attempt to solve the puzzle of the so-called "strong CP problem". This problem comes down to the fact that the QCD Lagrangian contains the following term:

$$\mathcal{L}_{\text{QCD}} \supset \bar{\Theta} \frac{g^2}{32\pi^2} G^{a\mu\nu} \tilde{G}_{a\mu\nu}; \quad (1.3)$$

where $G^{a\mu\nu}$ is the gluon field strength tensor and $\bar{\Theta}$ is a quantity closely related to the phase of the QCD vacuum. If $\bar{\Theta}$ were of order unity, as would naively be expected, this term would introduce large charge-parity (CP) violating effects, causing the electric dipole moment of the neutron to be $\sim 10^{10}$ times larger than experimental upper bounds permit. Therefore, to be consistent with observations, the quantity $\bar{\Theta}$ must be smaller than $\sim 10^{-10}$, even though this fine tuning is not natural.

They showed that by introducing a new global $U(1)$ symmetry that is spontaneously broken, the quantity $\bar{\Theta}$ can be dynamically driven toward zero, naturally explaining the small observed value. Such a broken global symmetry also implies the existence of a Nambu-Goldstone boson, called the axion. [5]

Constraints on the axion mass come from accelerator searches, red giants evolution, the supernova SN1987a and cosmology. The only mass range not yet excluded for the axion is $10^{-6} \text{eV} \leq m_a \leq 10^{-3} \text{eV}$. [5]

Such light and "invisible" axions can have very interesting consequences for cosmology. Being stable over cosmological timescales, any such axions produced in the early Universe will survive and, if sufficiently plentiful, could constitute the dark matter. For axions light enough to avoid the above mentioned constraints, however, the thermal relic abundance is predicted to be very small, and would only be able to account for a small fraction of the dark matter density.

1.2.3 WIMPs

Among all the possible species of dark matter, the Weakly Interacting Massive Particles (WIMPs) form a class of candidates capable of explaining this physics puzzle in a natural way. A WIMP is any particle that only directly interacts with matter via the gravitational and weak forces (not the normal "weak force" but something resembling it); has a large mass (typically on the scale of 1 GeV and above); and is stable on a time scale comparable to the age of the universe. [5]

In terms of theoretical expedience, what makes them such a popular dark matter candidate is the so called "WIMP miracle". This refers to the fact that by making minimal assumptions beyond an interaction cross-section on the weak scale, the WIMP relic density is actually comparable to the dark matter density measured in the Universe. Indeed, if WIMPs exist, they are a thermal relic of the Big Bang. As I mentioned at the beginning of Section 1.2, when the annihilation rate become

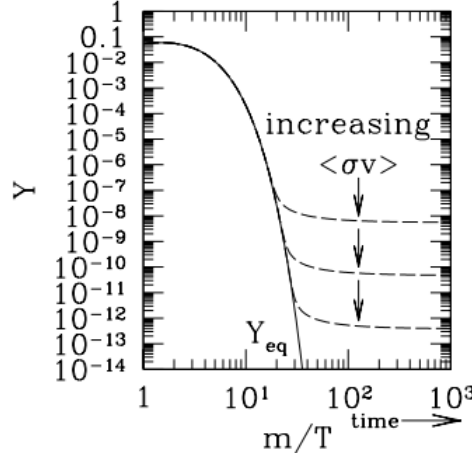


Figure 1.4: Typical evolution of the WIMP number density in the early Universe during the epoch of WIMP chemical decoupling (freeze-out). Credit: [9]

smaller than the expansion rate of the Universe, the production of that particle stops and we reach the so-called “freeze-out”. From that on, the number of WIMPs in a co-moving volume remained thus approximately constant, and that is the relic density we observe.

It is important to realize that the determination of the WIMP relic density depends on the history of the universe before the Big Bang nucleosynthesis (BBN). The BBN refers to the production of nuclei other than those of the lightest isotope of hydrogen, during the early phases of the Universe. Primordial nucleosynthesis is calculated to be responsible for the formation of most of the universe’s helium, along with small amounts of the hydrogen isotope deuterium, the helium isotope helium-3, and a very small amount of the lithium isotope lithium-7 [12].

We have no data from the epoch before the BBN. Therefore, to perform such a computation we need to make assumptions about the pre-BBN epoch which are: that the entropy of matter and radiation were conserved, that WIMPs were produced thermally, that they decoupled while the expansion of the universe was dominated by radiation and that, before they decoupled, they were in kinetic and chemical equilibrium. [9]

Given these assumptions the relic density of WIMPs can be obtained by solving the Boltzmann equation, combined with the law of entropy conservation:

$$\frac{dn}{dt} = -3Hn - \langle \sigma_{\text{ann}} \nu \rangle (n^2 - n_{\text{eq}}^2), \quad (1.4)$$

$$\frac{ds}{dt} = -3Hs. \quad (1.5)$$

where t is time, H is the Hubble parameter, n_{eq} is the WIMP equilibrium number density and $\langle \sigma_{\text{ann}} \nu \rangle$ is the thermally averaged total annihilation cross section. It is useful to combine eq.1.4 and eq.1.5 into one equation for $Y = \frac{n}{s}$ and $x = \frac{m}{T}$, with T the photon temperature, as the independent variable instead of time. [9] Moreover we shall use the relation between the Hubble parameter and the energy density ρ , according to the Friedman equation $H^2 = \frac{8\pi}{3M_{\text{P}}^2} \rho$, to rewrite this equation in the following form:

$$\frac{dY}{dx} = - \left(\frac{45}{\pi M_{\text{P}}^2} \right)^{-\frac{1}{2}} \frac{g_*^{\frac{1}{2}} m}{x^2} \langle \sigma \nu \rangle (Y^2 - Y_{\text{eq}}^2). \quad (1.6)$$

Eq. 1.6 can be numerically solved with the initial condition $Y = Y_{\text{eq}}$ at $x \simeq 1$ to obtain the present WIMP abundance Y_0 . The WIMP relic density is then computed such that:

$$\Omega_\chi h^2 = \frac{\rho_\chi^0 h^2}{\rho_c^0} = \frac{m_\chi^0 s_0 Y_0 h^2}{\rho_c^0} = 2.755 \times 10^8 Y_0 m_\chi / \text{GeV}, \quad (1.7)$$

where ρ_χ^0 and s_0 are respectively the present critical density and the entropy density. [9]

The evolution of Y as function of the temperature of the plasma is shown in Figure 1.4. Y tracks closely the Y_{eq} curve till the chemical decoupling temperature, when the annihilation rate drops, freezing the number of WIMPs per co-moving volume.

1.3 WIMPs Detection Techniques

WIMPs can potentially be detected by three complementary methods. In this section, we discussed briefly each of them and their experimental limits.

1.3.1 WIMP search through production

This first method aims at producing WIMPs in collisions of Standard Model particles at very high energies. This can be done at accelerators like the Large Hadron Collider (LHC) at CERN. WIMPs would be produced in pairs and would not be detected, therefore the typical signature is missing energy. The obvious limit of this experimental approach is given by the maximum energy reachable by interactions in the center of mass (not beyond the TeV scale). [13]

1.3.2 WIMP indirect search

Assuming WIMPs are their own anti-particles, they can self-annihilate, producing standard model products such as γ -rays and neutrinos. An excess of these particles in cosmic ray fluxes could be connected to dark matter and it can be detected with the use of advanced telescopes in orbit. Due to the rarity of such processes, the focus is on regions where the WIMP density might be higher, such as the centers of planets, stars, or galaxies. [14]

1.3.3 WIMP direct search

This method is based on the hypothesis that dark matter can interact with normal matter via some weak force boson carrier. The experimental signature in direct search detectors is a very tiny energy deposit released by the DM particle in the active volume of target nuclei. This energy is then converted in a detectable signal thanks to three different mechanisms: scintillation, ionization and phonons creation (i.e. temperature increase). Since direct searches look for rare events, they are heavily affected by the presence of backgrounds such as cosmic rays and natural radioactivity. The experiments are thus carried on in underground facilities in order to reduce the muon flux and fight the natural background radioactivity by means of active and passive shielding techniques.

Discussing all the different methods of direct detection, their experimental techniques and respective target nuclei used, is beyond the scope of this paper.

In the next section and the following chapters, we will discuss in more detail direct search experimental techniques and current limits in relation to the DarkSide Program, a WIMP direct search program at Gran Sasso National Laboratories in Abruzzo, Italy, (LNGS) which constitutes the main subject of this paper.

1.4 The DarkSide Program

The DarkSide program is one of the strongest experimental projects in the direct search for dark matter. Although the strength of the interaction of WIMPs is supposed to be very small, their thermal motion is expected to result in WIMP-nuclear collisions of sufficient energy to be observable by very sensitive laboratory apparatus. The DarkSide project attempts to detect WIMP-induced nuclear recoils using a dual phase Liquid Argon time projection chamber (TPC) operating at background-free acquisition mode. This goal is achieved by means of passive suppression and active rejection. [15]

DarkSide-10 The first DarkSide prototype was DarkSide-10, a technological demonstrator whose main aim was to measure the light detection capabilities of a TPC filled with LAr.

DarkSide-50 The second iteration of the program is DarkSide-50 which consists of three nested detectors: the Liquid Argon Time Projection Chamber (LAr TPC) which is the dark matter detector, the organic Liquid Scintillator Veto (LSV), serving as shielding and as anticoincidence for radiogenic and cosmogenic neutrons, γ -rays and cosmic muons; and the Water Cherenkov Detector (WCD), serving as a shield and as anti-coincidence for cosmic muons (see figure 1.5).

A dual-phase time projection chamber can detect both scintillation and ionization generated by recoils inside the target volume. Scintillation light (called S1) is the product of atomic de-excitation of Argon excimers, which are formed directly by the recoil. These recoils also produce ionization electrons which are drifted upward by a uniform vertical electric field into the gaseous Argon region where they produce a second light pulse (called S2) due to electroluminescence. The combination of the two pulses is very useful in rejecting background events, precisely determining the 3-D event positions of the event inside the TPC. [16]

The choice of using LAr as active target is due to its effectiveness in pulse shape discrimination. Indeed, Liquid Argon forms two different, nearly energy-degenerate, excimers: a short-lived (prompt) singlet ($\tau = 7$ ns) and a more stable triplet ($\tau = 1.6$ μ s). Both of them participate to the emission of the S1 scintillation light pulse but in different fractions if electron or nuclear recoils. In particular electron recoils, which constitute the largest source of background, produce events with a fraction of prompt light that is about 0.3, while for nuclear recoils this is around 0.7. The optimal and most convenient way to exploit this Argon property is to classify events on the base of their fraction of prompt light with respect to the total light in the first 90 ns (so called f_{90}). This

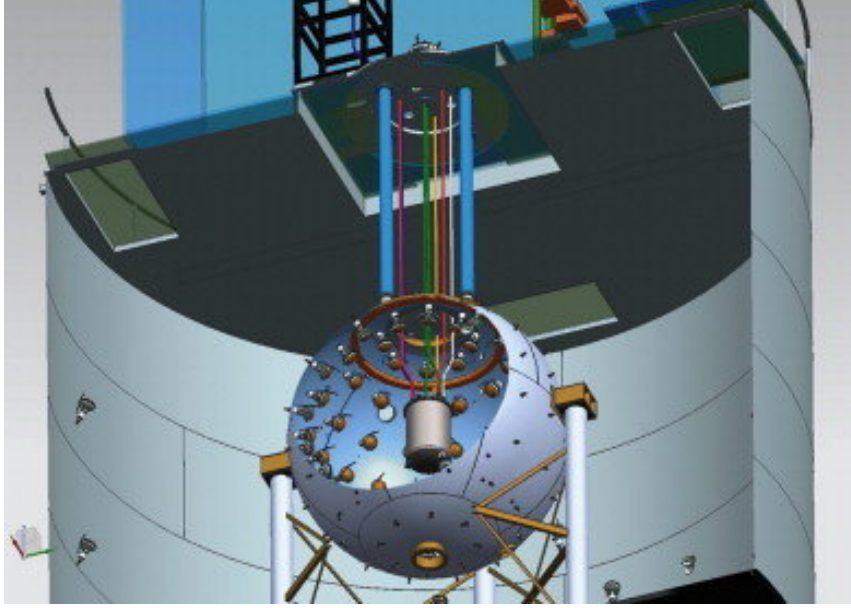


Figure 1.5: The nested detector system of DarkSide-50. The outermost gray cylinder is the WCD, the sphere is the LSV, and the gray cylinder at the center of the sphere is the LAr TPC cryostat, Credit: [16]

maximizes the separation among the distributions of ER and NR and allows us to effectively reject all ER events which we know represent the most conspicuous source of background.

DarkSide-20k The next step in the program is the construction of DarkSide-20k (DS-20k), a direct WIMP search using a LAr TPC with an active (fiducial) mass of 23 t (20 t) of UAr. The detector should achieve an exposure of 100 t yr, accumulated during a run of approximately 5 yr at background-free acquisition mode. To ensure the extremely low background needed to carry out the search, several technological developments had to be made. [17]

The most innovative design upgrade foreseen for DarkSide-20k is the shift in the TPC light detectors from the traditional PMT technology to the SiPM one. Silicon Photomultipliers (SiPMs) are innovative light detectors which combine the extreme sensitivity of standard photomultiplier tubes (PMT) with all the benefits of solid state devices, such as insensitivity to magnetic fields and very low radioactivity. Moreover, SiPMs can be more efficiently packed with higher geometrical fill factor and show a higher light detection efficiency. [18]

Given the increase in size of two orders of magnitude from DS-50 to DS-20k, the collaboration plans to build a prototype detector of intermediate size, DarkSide-Proto (DS-Proto), incorporating the new technologies for their full validation. The choice of the ~ 1 t mass scale allows a full validation of the major innovative technical features of DS-20k, including the mechanical and cryogenic design and the integration of the custom photodetector modules and the full read-out electronics and data acquisition chain. [17]

DarkSide-LowMass Most models predict dark matter WIMP masses near the electroweak scale of 100's of GeV/c^2 . [19] However, in recent years it has been shown that many production mechanisms that explain the observed DM relic abundance are compatible with dark matter particle

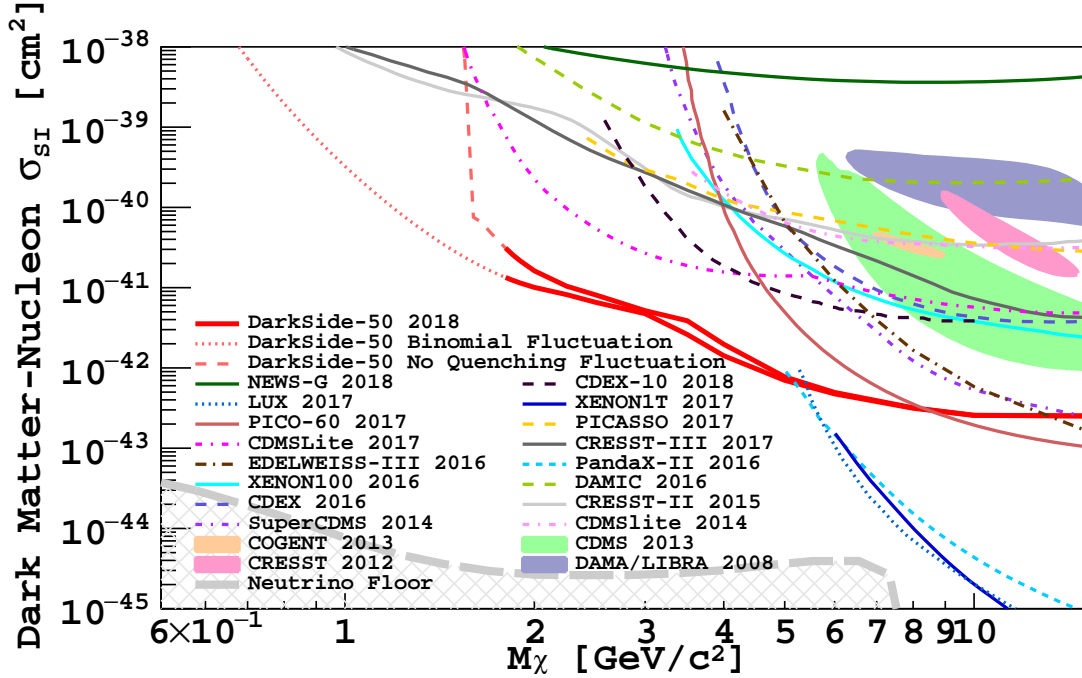


Figure 1.6: The 90 % C.L. exclusion curves for the binomial fluctuation model (red dotted line) and the model with zero fluctuation in the energy quenching (red dashed line). For masses above $1.8 \text{ GeV}/c^2$, the 90 % C.L. exclusion is nearly insensitive to the choice of quenching fluctuation model. Below $1.8 \text{ GeV}/c^2$, the two exclusion curves rapidly diverge because of the effective threshold due to the absence of the fluctuations in the energy quenching process. Credit: [19]

masses $\leq 10 \text{ GeV}/c^2$ if a significant asymmetry between dark matter and their anti-particles existed in the early Universe. [20]

In this regard, the results published in early 2018 from a 532.4 live-days campaign of the DS-50 detector played a crucial role. The outcome of the high-mass WIMP dark matter search was a null result. On the other hand, the extremely low background, high stability, and low 0.1 keV_{ee} analysis threshold of DS-50, [21] enabled a study of very-low energy events, characterized by the presence of the sole ionization signal (WIMPs in this mass range produce nuclear recoils well below 1.66 keV_{ee} , where the efficiency for detecting the S1 signal is too low and PSD is moreover not available). [19]

This analysis resulted in the world-best limit for low-mass dark matter searches in the mass range $1.8 \text{ GeV}/c^2$ to $6.0 \text{ GeV}/c^2$ as shown by C.L. exclusion curves shown in Figure 1.6. In section 4.3 we will discuss more in details how to obtain C.L. exclusion curves and what they actually represent but here what it is important to understand is simply that everything above each curve corresponds to a combination of dark matter mass and cross section (m_χ, σ_χ) that has been excluded. It is clear then that the red curve, representing DarkSide-50, is the one with the largest area above and therefore the one that obtained the best limit, up to a 90 % confidence level as shown in figure.

Based on the recent success in low-mass searches, the Collaboration has decided that it will propose to LNGS the construction and operation of DarkSide-LowMass (DS-LM), a search specialized for discovery of dark matter in the low mass region, exploiting elements of the DS-Proto detector.

The purpose of this paper is indeed to investigate the limits of the DM-LM search by studying

changes in both the geometry and composition of the detector in order to optimize its sensitivity, given the current state of the technology.

Chapter 2

The Dark-Side LowMass Detector

In this Chapter, at first we will discuss in detail the geometry and functioning of the elements of a DS-Proto like detector. Then I will describe the proposal for a new detector, the DS-LowMass detector, which exploits the main features of the DS-proto detector with a few adaptations to optimize the search in the low-mass range. Finally, I will introduce all the sources of background, with emphasis to those relevant to the low-mass search.

2.1 The DS-Proto Detector

In this section, we consider the design of the detector which will be commissioned for DarkSide-Proto. This Detector is composed by three elements: the LAr TPC, the cryostat and LSV.

The LAr Time Projection Chamber (TPC) The LAr TPC is the dark matter sensitive detector and central element of the experiment, and it must satisfy many requirements. Here we list the most relevant for low mass dark matter search:

- to be realized only with radiopure materials;
- to provide uniform drift, extraction and electroluminescence fields and gas pocket thickness for high resolution of S2 signals;
- to provide a very reliable $x - y$ position reconstruction. Given the high number of channels and their dynamic range of ~ 100 PE, a very good spatial $x - y$ resolution, in the range 5-20 mm, is expected.
- to allow effective circulation of LAr to maintain purity.

The geometry is that of an octagonal parallelepiped of edge 30 cm and height 58 cm.

The TPC will operate in two-phase mode, using both the liquid and gas phases of argon. It will be filled with underground argon UAr extracted from Doe Canyon (Colorado), since such argon has a concentration of ^{39}Ar a factor $(1.4 \pm 0.2) \times 10^3$ below that of atmospheric argon. [22]

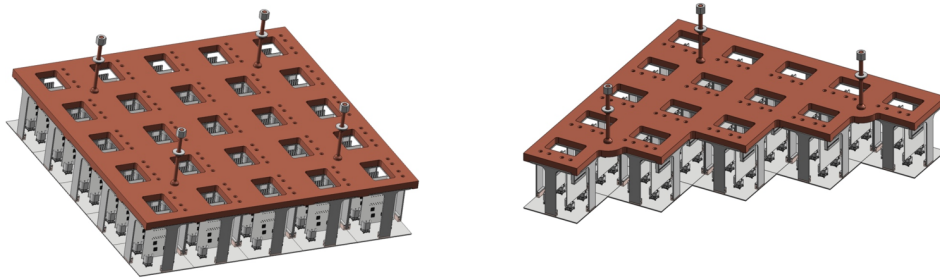


Figure 2.1: A single SQB (left) and a single TRB (right). SQBs and TRBs are assemblies of tiles serving as building blocks of the octagonal readout planes. Credit: [17]

The active LAr volume is defined by an acrylic window at the bottom of the detector, coated with ITO (transparent conductive indium-tin-oxide) and serving as cathode, a grid just below the liquid surface and a reflecting surface with an octagonal shape on the sides. The thin argon gas pocket above the liquid surface is bounded at the top by another acrylic window coated with ITO, which in this case serves as anode. A high voltage is applied between the cathode and the grid to produce a vertical electric field to drift the ionization electrons created at the interaction site upward. An independent potential between the grid and the anode creates the fields to extract the electrons into the gas and accelerate them to create secondary scintillation (i.e., the S2 signal). [17]

To maximize the light yield, all inner surfaces delimiting the active Argon volume are coated with the wavelength shifter tetraphenylbutadiene (TPB), which absorbs the 128 nm scintillation light and reemits it with high efficiency in the blue region (~ 420 nm). The converted one will then be detected by two densely packed arrays of SiPM-based PDMs, placed one above the anode plane and below the cathode plane of the LAr TPC. The two detection planes consist of 185 photon detection channels each. A single readout channel consists of a 50×50 mm² SiPM tile assembly, where 24 single devices are joined together to form a single photodetection unit. The tiles are grouped in two different types of larger mechanical units called the SQuare Board (SQB) and the TRiangular Board (TRB), as shown in Figure 2.1. The SQB and TRB are used to form the full readout octagonal planes. [17]

These arrays of SiPM photosensors which view the active LAr volume through the acrylic window. The S2 signal is concentrated in the top array and within a few SiPM tiles around the transverse position of the ionization drift, thus yielding a precise x and y location. On the other hand, at very low energies (the ones we are interested in for a low mass dark matter search) S1 signals are too small or even absent to provide a measurable signal, therefore we cannot use the drift time (the time between the S1 and S2 signals) to determine the z -location of the event in the LAr TPC. [17]

The electric field configuration inside the LAr TPC consists of an active LAr volume with an applied uniform drift field of 200 V/cm, 3 mm of LAr above the grid with an extraction field of 2.8 kV/cm and a 7 mm thick argon gas pocket with an electroluminescence field of the order of 4.2

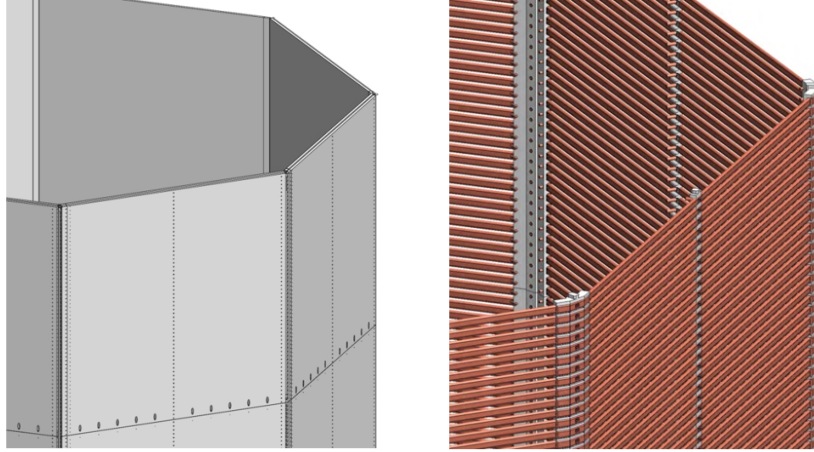


Figure 2.2: Field cage (left) and reflector panels (right) of the LAr TPC. Credit: [17]

kV/cm. The uniformity of the electric drift field is provided by a field cage consisting of octagonal field shaping rings, as shown in Figure 2.2, equally spaced along the z -axis and biased with a uniform voltage gradient. [17]

The side boundaries of the active volume are defined by an octagonal assembly of sixteen highly-reflective acrylic panels. Eight acrylic panels form an octagon that is stacked onto another acrylic octagon, as shown in Figure 2.2. This design simplifies the fabrication, since large panels of acrylic are not readily available. the acrylic panels will be 1.5 cm thick and coated on the inner surface with $200 \mu\text{g}/\text{cm}^2$ of TPB layer.

In figure 2.3, we can view a 3D rendering of the DS-Proto LAr TPC as described above.

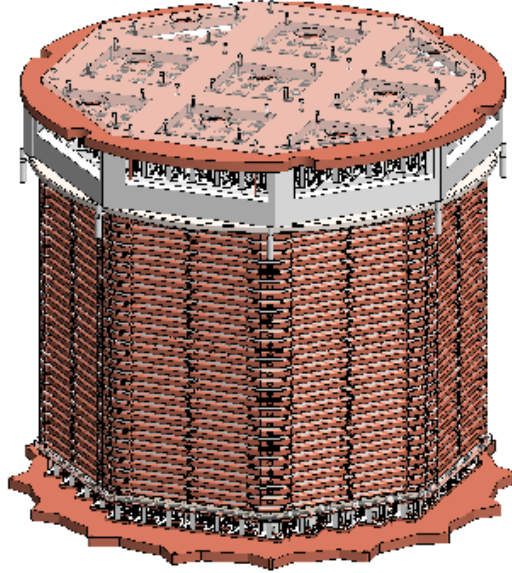


Figure 2.3: 3D- rendering of DarkSide-Proto LAr TPC. Credit: [17]

Cryostat The Cryostat consists of a 4π vacuum-insulated vessel made of three separate parts, the top assembly, the inner cryostat vessel, and the vacuum insulation vessel. Its main purpose is that

to isolate the LAr target from the external environment in order to keep it cool and purified. [17]

The top assembly is formed by an outer dome and an inner dome mechanically linked with solid low-thermal-conduction rods. The outer dome of the top assembly has a flange that matches the insulation vessel flange and uses a metal o-ring as the vacuum seal. The inner dome has a flange that matches the inner cryostat vessel and uses a V-groove indium wire seal. [17] The thickness of the inner and outer cryostat vessel is respectively of 1.25 cm and 1.75 cm. All the elements of the Cryostat are made of Stainless Steel whose total mass can be estimated to be 1.234×10^3 kg. The estimation, done in this work, is simply the result of considering both the inner and outer vessel of the cryostat as normal cylinders without domes at the top and bottom in order to facilitate the computation of the total volume which is then multiplied by the density of Stainless Steel (7.7×10^3).

In Figure 2.4, we can view a 3D rendering of the cryostat as described above.

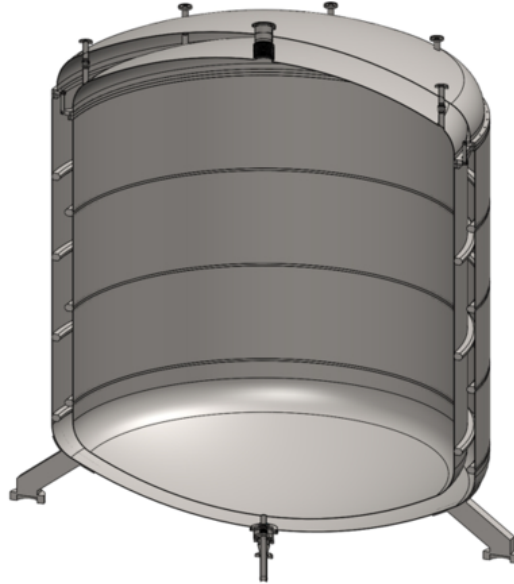


Figure 2.4: 3D- rendering of DarkSide-Proto cryogenic Cryostat. Credit: [17]

Liquid Scintillator Veto (LSV) The LSV is a 4.0 m diameter stainless steel sphere filled with 30 metric tonnes of boron-loaded liquid scintillator and is an highly efficient active veto for neutrons. [23] Neutron tagging is performed searching both for thermalization and neutron capture signals, with a measured efficiency $\geq 99\%$. [24]

The sphere is lined with Lumirror, a reflecting foil used to enhance the light collection efficiency. An array of 110 Hamamatsu R5912 LRI 8" PhotoMultiplier Tubes (PMTs) is mounted on the inside surface of the sphere to detect scintillation photons (see Figure 2.5).

2.2 The DS-LowMass Detector

As explained in Section 1.4, the choice of using LAr as active target was mainly due to its effectiveness in pulse shape discrimination between electron and nuclear recoils (ERs and NRs),



Figure 2.5: Internal view of the LSV neutron veto from its top port with the PMTs directly mounted on the surface of the sphere. Credit: [23]

allowing us to effectively reject all ER events which, as we will see more in detail in Section 2.3, represent the most conspicuous source of background. Therefore, the main and most dangerous background left was that of neutrons (the main source of NRs) which is why in the DarkSide detectors the neutron vetoes outside the TPC have always played a crucial role.

However, at low-energies the separation in the values of f_{90} (go back to Section 1.4 for its definition) for ERs and NRs disappears and they become almost indistinguishable. Therefore, in the context of a search in the low-mass range, where pulse shape discrimination (PSD) is impossible, and since the mechanisms by which neutrons are produced (causing NRs) are extremely rarer than all the other mechanisms that lead to ERs, neutrons constitute only a minimum, almost irrelevant, fraction of the total background budget. The role of an active neutron veto loses its importance and thus forces us to rethink the geometry of the detector.

The DS-LowMass detector, which I propose in this paper, is meant to optimize the search for dark-matter in the low-mass range. This detector is composed by two elements: the LAr TPC and a cubic LAr Box.

LAr TPC The LAr TPC has the same features as the one described in the previous section with only one change in the thickness of the acrylic panels which is reduced to 0.5 cm. This choice was made in order to further lower the activities of the radioisotopes by which is composed (see Section 2.4 for more details) and preserve the solidity of the TPC.

Cubic LAr Box (CLArB) Following our discussion above, it is clear that a neutron veto, like the LSV, is completely useless for the purpose of our search.

We can substitute it with a large cylindrical acrylic box of 2.5 cm thickness, filled with LAr which acts as passive shield for decays of radioisotopes from the external environment. The addition of the CLArB also allows us to eliminate the cryostat around the TPC, which constituted one of the main sources of background, by fulfilling the goal of isolating the LAr target from the external

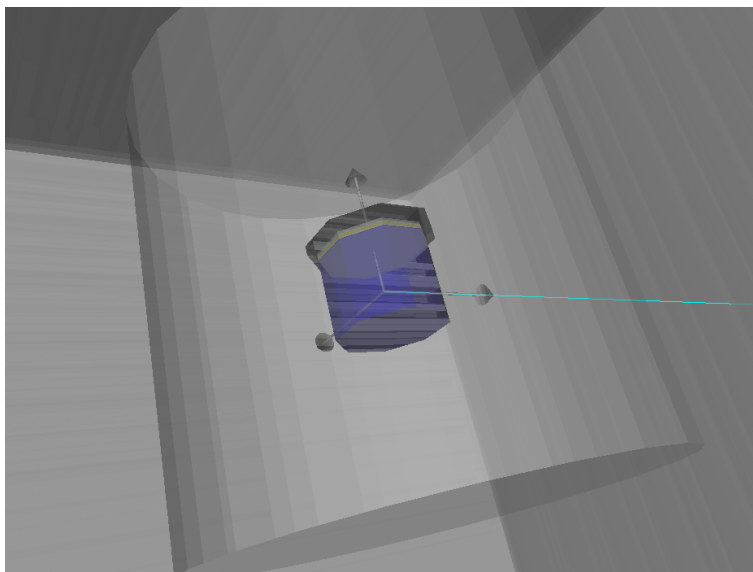


Figure 2.6: 3D-rendering of the proposed geometry for the DS-LowMass Detector. The large silver cylindrical box is the CLArB of thickness 2.5 cm. The small blue cylinder, enclosed in the CLArB, is the TPC filled with LAr. Finally at the top and bottom of the TPC we can view the arrays of SiPM-based PDMs.

environment to keep it cool and purified.

In Figure 2.6, we can view a 3D rendering of the entire detector as described above.

2.3 Sources of Background

Any signal detected inside the TPC that is not caused by a WIMP interaction with LAr is considered as a source of background. All the possible known backgrounds can only arise from the reactions generated inside the detector of 6 different particles: neutrons, γ -rays, X-rays, β -rays, α -particles and muons. The mechanisms that controls these sources of background are described below.

2.3.1 Cosmogenic Muons

Cosmic rays constantly bombard Earth's atmosphere and produce showers of particles at high altitudes. Some of the most long-lived of them, typically muons, can reach the ground level and even keep traveling deep in the terrestrial crust for hundreds of meters before decaying or interacting.

Some of these highly relativistic muons thus can still penetrate down into the detector and produce a large amount of scintillation light in it. They are not directly a large source of background, since they produce too large of a signal to look like a WIMP. However, through their interactions with the rocks and the surrounding laboratory materials, they can produce many other particles, including high energy neutrons. [25]

Indeed, most cosmogenic neutrons are produced by these photo-nuclear reactions and their production tends to be in prompt coincidence with the passing muons. That said there is a class of cosmogenic neutrons that are delayed from the prompt signals. These are the product of the decaying

unstable nuclei with long half-lives left by the photo-nuclear reactions induced by muons. [25]

2.3.2 β -Decays

A β -decay is a type of radioactive decay in which a β -ray (fast energetic electron or positron) and an antineutrino or neutrino are emitted from an atomic nucleus. For example, a β -decay of a neutron transforms it into a proton by the emission of an electron and an antineutrino.

Since many radiogenic materials undergo β -decays, a lot of β -rays can end up inside the TPC and, since they are a charged particle, they can directly produce a detectable scintillation light. [25]

2.3.3 α -Decays

Many nuclei with $Z > 82$ can become more stable by emitting an α -particle. Due to their high charge and consequent high stopping power, in most materials, these α particles tend to travel very short distances. [26] This short distance means that alpha decays that take place in the various detector materials will tend not to leave a signal in the TPC.

However, some of these heavy nuclei may be found in higher concentrations on the inner surfaces of the detector in contact with the LAr. In this scenario the background seen by the detector can result directly from the signals produced by the emitted α -particles, or by the recoiling daughter nucleus after the decay. These kinds of backgrounds are referred to as **surface** background. [26]

2.3.4 γ -Rays and X-Rays

γ -rays come from nuclear transitions after some sort of nuclear decay or reaction. They are the product of these nuclear de-excitations which are typically preceeded by β -decays which produce an excited state of the daughter nucleus. These γ -rays can also be produced by α -decays, even if these transitions are less common. [25]

x-rays, on the other hand, typically come from lower energy atomic transitions as atomic electrons relax to lower energy levels. Inside the TPC, both γ and x-rays may transfer energy to electrons through both Compton and Photoelectric effects. These electrons will then scintillate as they slow down in the LAr.

2.3.5 Neutrons

Neutron backgrounds come from three primary sources. The first source is cosmogenic as a result, as I mentioned earlier, of photo-nuclear reactions triggered by highly relativistic muons. The other two mechanisms by which neutrons are produced in the TPC are by spontaneous fission processes, and (α ,n) reactions.

Spontaneous fission is the process by which a nucleus splits into two smaller nuclei. Conservation of baryon number tells us that A must be conserved but it does not specify how the nucleons are divided between the fragments. Due to the nature of this process, at least one of the fission fragments will be left with too many neutrons to be stable causing their emission. A very important feature

is that the neutrons produced by spontaneous fission tend to be accompanied by many high energy γ -rays, carrying away excess energy from the fission fragments.

On the other hand, the mechanism behind an (α, n) reaction starts with an α -particle typically produced from the decay of a radioisotope in the relevant material. If the incident α -particle has enough kinetic energy (generally more than ~ 30 MeV [27]), it can scatter directly off the nucleons in the target nucleus, and “knock” a neutron out this way.

It is important to notice that, as emphasized in Section 2.2, for dark matter searches in the low-mass range, neutrons are basically an irrelevant source of background. That said, I believe it was still important to describe the mechanisms by which they are produced to provide a complete description of all the processes that happen inside the detector.

2.4 Relevant background-producing Radioisotopes

As we have seen in the discussion above, all the several backgrounds producing a signal in the sensors have only two possible origins: cosmogenic, due to the interactions caused by cosmic ray muons and radiogenic, which come from several radioactive processes around and inside the detector. It becomes therefore clear the importance to have a deep understanding of all the possible sources of radioisotope activity in the detector. Here it follows a list of the most relevant radioisotopes that produce a measurable signal in the TPC.

2.4.1 ^{39}Ar

^{39}Ar is a naturally occurring radioisotope of argon with a half-life of 269 yr [28]. It is produced from cosmic ray activation of ^{40}Ar , which explains its lower abundance in UAr. Since this background is intrinsic to the argon itself, ^{39}Ar decays within the detector’s sensitive argon volume will deposit all of their energy into the argon.

The decay produces β -particles which in turn produces scintillation in the LAr causing the measurable signal. The danger of a high ^{39}Ar concentration is also that it may result in a pileup of ^{39}Ar decays which would drastically reduce the live time of the experiment by constantly triggering the detector on these kinds of decays, interfering with the detector’s ability to acquire other events. [29]

2.4.2 ^{60}Co

^{60}Co is not a naturally occurring isotope of cobalt. While small amounts of it may be produced due to cosmogenic activation, its relatively short half-life of 5.27 years [28] means that it does not naturally accumulate in any appreciable amount. Most of ^{60}Co present today is synthetic and is incidentally present in steel, entering the manufacturing process in the form of contaminated scrap. [30]

^{60}Co undergoes β -decay which leads to the production of two relatively high energy γ -rays which can then result in single, or multiple, LAr scatters. [31]

2.4.3 ^{40}K

Due to its long half-life of over 1 billion years, most of the ^{40}K in the earth and sea water has not yet decayed, giving ^{40}K a natural abundance of 0.012% [28]. Since potassium has a very high natural abundance, ^{40}K is present in most metal ores and therefore also in the non-scintillating components of the detector (for instance the stainless steel).

^{40}K is one of the most abundant γ -ray emitters naturally present in common detector materials. The reactions by which these γ -rays are emitted may be followed by x-rays as the atom relaxes, or by the emission of a 2.66 keV Auger electron. [25]

These x-rays are very low energy and are generally not a problem for experiments like DarkSide-50 with energy thresholds above 10 keV_{ee}. However, they are important for experiments looking for low mass WIMPs with lower energy thresholds.

2.4.4 ^{232}Th

^{232}Th is naturally present in the crust of the earth and has a half-life of 1.4×10^{10} yr [28]. Due to its presence in rock, trace amounts of ^{232}Th tend to be present in most metal samples.

It is the head of the ^{232}Th decay chain, which includes a wide array of important radioisotopes. This decay chain produces γ -rays, which can result in single or multiple LAr scatters, and neutrons which may then scatter in the TPC. The process of neutron production can happen via spontaneous fission or via the subsequent (α, n) reactions triggered by α -decays resulted from the ^{232}Th decay chain. [25]

2.4.5 ^{238}U

Uranium is naturally present in the crust of the earth with a half-life of 4.5×10^9 yr [28]. As a result, most metals mined from the earth will have some trace level of ^{238}U contamination.

Much like ^{232}Th , the ^{238}U decay chain contains many radioisotopes that can constitute various γ -rays and surface backgrounds. It can also produce fission neutrons and (α, n) neutrons.

In the case of ^{238}U it is important to differentiate between the upper and lower parts of the chain. The ^{238}U upper chain ($^{238}\text{U}^{\text{upper}}$) mostly produces low energy γ -rays; meanwhile the ^{238}U lower chain ($^{238}\text{U}^{\text{lower}}$) produces gamma-rays with significant energies up to 2.5 MeV.

2.4.6 ^{235}U

^{235}U is a naturally occurring isotope of uranium and is nearly inevitably present in trace amounts of metal samples. Although it is always present in smaller concentrations than ^{238}U , the ^{235}U decay chain contains higher energy α -decays which are a source of neutrons from the subsequent (α, n) reactions [28]. ^{235}U can also undergo spontaneous fission but the main product of the ^{235}U decay chain is still given by low energy γ -rays which can then result in a single, or multiple, LAr scatters. [31]

Chapter 3

Simulations and Analysis

It is useful after two long introductory chapters to remind ourselves the purpose of this research is. The end goal, as clearly stated in the title of this paper as well, is that to investigate the physical reach of an optimized double phase TPC for searches of dark matter in the low-mass range.

To accomplish this, we need to obtain the N_{e^-} spectra for each of the sources of background. A N_{e^-} spectrum plots the number of total events (y -axis) with the amount of electrons generated per event (x -axis). By matching these spectra with the N_{e^-} spectrum of dark matter for possible values of its mass and cross section we can evaluate to which DM-masses the detector is sensitive.

Given that the two detectors we consider in this paper do not exist yet and therefore cannot be tested experimentally, we need to produce simulations in order to attain these spectra. These simulations have to take into account all the details of the geometry of the detector, the activity of the radioisotopes of interest and how they decay and interact inside each of the components of the detector. To run these simulations, I used the Geant4 MonteCarlo package named G4DS, already adopted to estimate the background for DarkSide-50. A detailed description of the package and the simulations generated follows in Section 3.1.

The crucial and final step to actually get the N_{e^-} spectra is composed of two actions: first of all, convert the information provided by the simulations in data we would observe during a real experiment; then apply cuts to exclude as much background events as possible without affecting excessively the signal acceptance. This is accomplished by means of an analysis process which I discuss in depth in Section 3.2.

3.1 MonteCarlo (MC) Simulations

3.1.1 G4DS: The MC Package for the DarkSide Program

G4DS is a simulation code developed by the DarkSide collaboration based on the Geant4 MC package. Generally, MC methods comprehend a varied class of algorithms whose essential idea is that of using randomness to solve problems that might be deterministic in principle. [32] In particular in our case, G4DS is a toolkit designed with a modular architecture in order to include a

full description of all the detectors belonging to the DarkSide program. It includes detailed geometry descriptions, properly tuned physical processes, and the full optical propagation of photons produced by scintillation in liquid argon and electroluminescence in gaseous argon. [33]

The code also embeds a rich set of particle generators that allows simulations of beta decays, single and chain radioactive decays, cosmic muons and neutron fluxes. [33]

3.1.2 MC Simulations Generated

I used the G4DS MC package just described to generate a large number of the nuclei of the radioisotopes presented in Section 2.4. These nuclei were generated at rest, in random positions inside the components of the TPC.

The main element of the detector excluded from the simulations is the Veto System. Indeed, the basic idea of a Veto is to use anti-coincidence to reject events of background. However, the only way to cause a simultaneous scintillation both in the Veto and inside the TPC is through events at high energy or via neutron multiple scatterings which are of no interest in this research, thus making simulations in the Veto useless.

The choice of the number of simulations to generate per radioisotope was simply based on statistical considerations, to attain a continuous N_{e^-} spectrum with sufficiently populated bins. Table 3.1 contains the complete list of the location and number of events generated per radioisotope. As we can see, all the radioisotopes, apart from ^{39}Ar which is only present in LAr, are generated in the materials composing the boundaries of the TPC (both the reflector panels on the sides of the TPC, and the window at the top and bottom of the TPC); in the cryostat and PDMs, hereforth referred to as “SiPMs”.

Rad.Chain	Det.Component	Simulated
^{238}U	Reflector	1×10^9
^{238}U	Window	1×10^9
^{238}U	Cryostat	5×10^9
^{238}U	SiPM	5×10^8
^{235}U	Reflector	3.3×10^8
^{235}U	Window	1×10^8
^{235}U	Cryostat	2×10^9
^{235}U	SiPM	1.2×10^8
^{232}Th	Reflector	5×10^8
^{232}Th	Window	1.5×10^8
^{232}Th	Cryostat	1×10^9
^{232}Th	SiPM	1.2×10^8
^{40}K	Reflector	5×10^8
^{40}K	Window	3×10^8
^{40}K	Cryostat	1×10^9
^{40}K	SiPM	2.5×10^8
^{60}Co	Reflector	1.5×10^8
^{60}Co	Window	1.2×10^8
^{60}Co	Cryostat	3×10^8
^{60}Co	SiPM	1×10^8
^{39}Ar	LAr	5×10^7

Table 3.1: Full list of the radioisotopes simulated in each of the 5 detector components: the reflector panels around the TPC (Reflector); the windows at the top and bottom of the TPC (Window); the Cryostat and the SiPMs. Here there is no distinction between $^{238}\text{U}^{\text{up}}$ and $^{238}\text{U}^{\text{low}}$ because I simulate the same number of events for both.

3.2 The Analysis Process

3.2.1 From MC Simulations to Observables

The first step of the analysis process is to convert the information we have from the simulations into data we would actually observe during an experiment.

What we get from the MC simulations are clusters of events. A cluster is defined as one or more energy deposits which occur at a distance not greater than 1 mm on the z-axis and within a time window of $10\ \mu\text{s}$. This time window opens with the first energy deposition. The all point of this “clusterization” is to eliminate the artificial discretization of energy deposits carried by the G4DS, which treats continuous energy losses (like ionization) as successive finite steps.

From each of these clusters we get several information of which the most relevant to our scope are energy and position. However, during a real experiment, we do not observe these values. Instead, what we would measure is simply the light of S2 captured by the PDMs. From this, we would be able to determine how many electrons were generated during the interaction and the x-y position of such interaction given the distribution of the light in the SiPMs.

Therefore, to convert the information of the MC simulations into observables we need to proceed

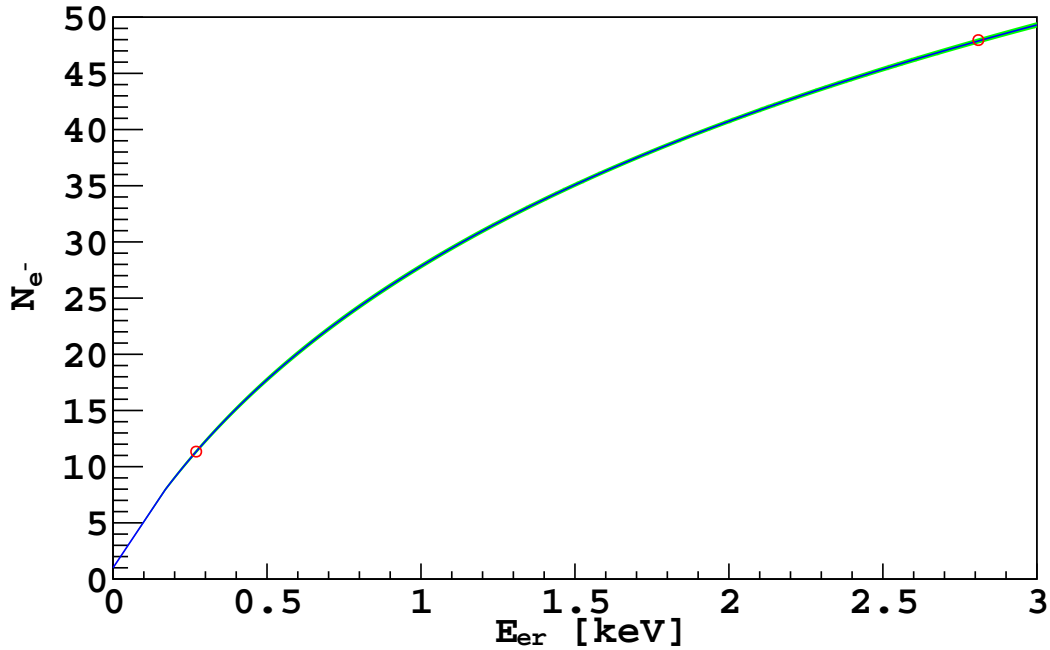


Figure 3.1: Calibration curve used to convert electron recoil spectra to ionization spectra. Below $8\ N_{e^-}$, it is assumed there is no recombination and use a straight line that intersects $N_{e^-} = 1$ with a slope determined by the ratio of the number of excitations to ionization, $N_{ex}/N_i = 0.21$, measured in ref. [34] and the work function measured in ref. [35]. Above this point, the effects of recombination are included by fitting the Thomas-Imel model [36] to the mean N_{e^-} measured for the 2.82 keV K-shell and 0.27 keV L-shell lines from the electron capture of ^{37}Ar . In order to get good agreement between the model and data, we multiply the model by a scaling factor, whose best-fit value shifts the curve up by 15%. This scaling factor can be interpreted as the agreement between our measured N_{ex}/N_i and work function and the literature values. The green band shows the statistical uncertainty of the fit. Credit: [37]

backwards. Given the energy deposited of the cluster, we need to convert it into number of electrons generated (N_{e^-} spectrum).

This is accomplished by a scale conversion from electron recoil spectra to ionization spectra based on a fit to low-energy peaks of known energy, as shown in Figure 3.1 and described in ref. [19]. The resulting ionization spectra are then smeared assuming the ionization yield and recombination processes follow a binomial distribution. [37]

To convert the position of the cluster in $S2_x$ and $S2_y$ we simply need to add a Gaussian smearing since in reality the distribution of the light in the SiPMs allows us to determine the x and y position only up to a certain resolution which in this paper we consider to be of about 1.5 cm.

We completely disregard the location on the z -axis of the cluster since, as clearly explained in Section 2.1, at low-energy we are only able to measure S2 signals and thus cannot use the drift time (the time between the S1 and S2 signals) to determine the z -location of the event.

3.2.2 Selection Cuts

After the conversion of the MC simulations into observables we need to think about the experiment as we would in a real-life situation.

In this scenario, we actually do not know what particles have interacted inside the detector and in what way. All we observe is a series of S2 signals of different intensity and distribution and what we are asked is to perform cuts in order to eliminate all kinds of events which clearly represent an undesired source of background. The selection cuts I made in this research are three and are described in detailed in the paragraphs below. Also, in Figure 3.2 we can see how these cuts effect individually the shape of the N_{e^-} spectra taking as an example the N_{e^-} background spectrum in the SiPMs.

Single Scatter Cut (SS cut) The Single Scatter cut is meant to eliminate all those events that occur too close to each other and thus those interactions where we observe more than one scatter. The idea behind this cut is that, given the rarity of any possible interaction between particles of the standard model and DM particles, such events would definitely only produce a single scatter. In this research, we are producing single events without worrying about pileup, therefore this time constraint results in cutting all those events with a number of clusters greater than 1 ($N_{\text{clus}} > 1$).

Energy Deposition Cut The Energy Deposition cut is straightforward. Since we are looking for dark matter scattering at low energy we are not interested in any event which produced too many electrons. Specifically we cut all the events that generate more than 50 electrons ($N_{e^-} < 50$). This is reflected in the fact that all the plots presented in this paper are formatted in the range from 0 to 50 N_{e^-} .

Fiducial Cut As explained in Section 2.3; one of the main sources of background comes from the decay of heavy nuclei found in higher concentrations on the inner surfaces of the detector in contact with the LAr.

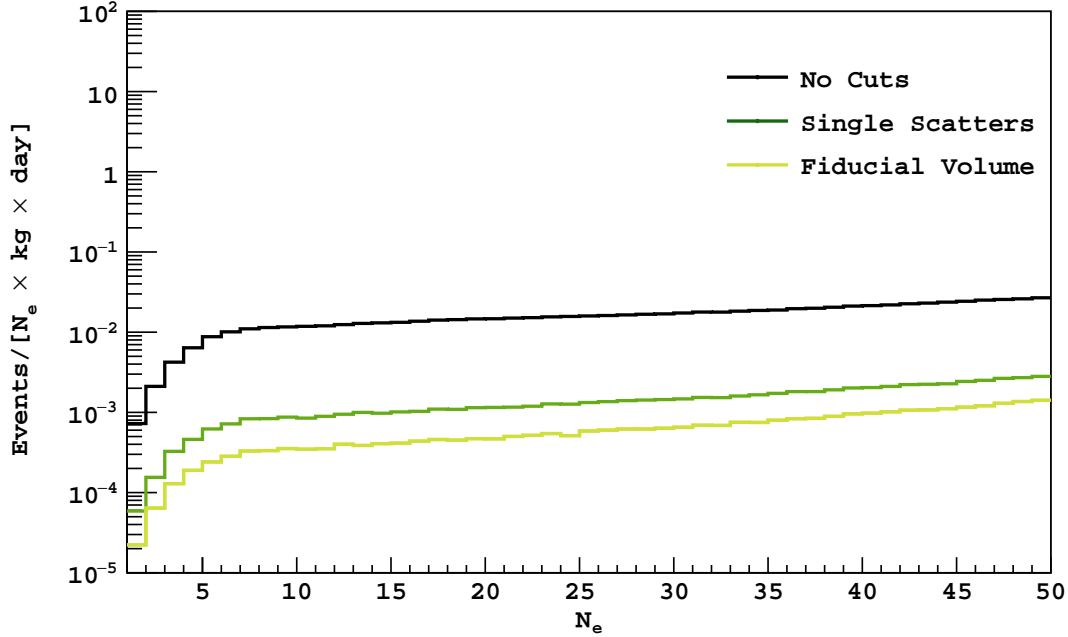


Figure 3.2: The plot shows the N_{e-} background spectrum in the SiPMs before and after each of the selection cuts is individually applied. The SS cut is the one that lowers the curve the most from approximately 10^{-2} to 10^{-3} background events expected per kg per day. The fiducial cut lowers the curve even more of about another half a order of magnitude. The energy deposition cut does not show up because the plot was already designed to show only values in the range between 0 and 50 N_{e-} .

The Fiducial cut is exactly meant to avoid these kinds of events which happen near the surface of the TPC. In particular, we disregard all events within a 10 cm distance from the edges of the TPC for a final fiducial mass of LAr of 181.1 kg.

3.2.3 Normalization

The process of the selection cuts just described above is crucial in order to understand the fraction of total events we are able to reject starting from the number of simulated ones. That said, the number of simulated events per radioisotope has no physical significance. In reality, the number of events per radioisotope that will occur depends on the activity of each of these elements inside the components of the detector.

Therefore, to obtain the finalized N_{e-} spectra we need to normalize these curves based on the actual expected activities of the radioisotopes. The basic idea of the normalization is that to multiply the fraction of events that survived the analysis cuts by the total number of events we expect to see per day per kg inside each component of the detector.

To accomplish this result it becomes crucial to know the total activity of each radioactive element in the materials that compose the detector. In fact, known these we only need to multiply them by the number of seconds in 1 day (86400 s) and divide them by the fiducial mass of LAr in the detector ($m = 181.1$ kg).

In the same way, the total activity is simply given by another multiplication, in this case between the activity per kg inside a certain material times the mass of that material in the detector. In table 3.2 I included all the values of the masses of the materials for both of the detectors we consider in this research. To obtain these values, I multiplied the volume of each component of the detectors for the density of the corresponding material, information both provided by G4DS.

On the other hand, in table 3.3 I summarized all the data currently available on the activity per kg of the radioisotopes inside each of the materials of the detectors. These values are taken from the DarkSide materials database [1], a database of the DarkSide program constantly updated with new measurements.

The “<” symbol for both ^{40}K and ^{60}Co in the table serves to indicate that the values presented only represent upper limits and not accurate measurements of the activity. Moreover, the limit on the activity of ^{40}K in acrylic was taken from the requirements made by the JUNO collaboration described in ref. [38].

The reason why we lack accurate measurements of the activities of both ^{40}K and ^{60}Co is because their interaction in LAr produces ERs which were easily rejected in searches for high mass dark matter by means of pulse shape discrimination. These events were therefore almost completely cut during the analysis process and never represented a problem to worry about. Now, in a low-mass DM search, where pulse shape discrimination cannot be performed, they indeed represent a huge source of background that cannot be ignored.

Finally, the activity for the SiPMs is given per PDM and it was computed by summing over the single activity per kg of each of the materials that compose the PDM times their respective mass. For a more detailed description of this computation refer to Appendix A.

By looking at table 3.3, we immediately notice two essential differences between the two detectors: the reduction in the activity of ^{39}Ar in LAr and of all the other radioisotopes in the SiPMs. The improvement in the activity of ^{39}Ar in LAr of two orders of magnitude is an estimate of the expected performance of the ARIA project, a 350-metre-tall distillation tower, still in construction at CERN, that will be used to purify liquid argon for the DarkSide detectors. [39]

In regards to the SiPMs, there is still an R&D process carried on at LNGS. The latest results collected show the possibility to reduce the number of 50 M Ω resistors, which as shown in table A.1 represent the main source of background in the SiPMs, from 52 to 8. Moreover, together with this reduction in the number of the 50 M Ω resistors, they believe they can also reduce the mass of all the other components of the SiPMs without effecting the performance requirements of DarkSide. The reduction, everything considered will be of a factor between 5 and 10. These are only preliminary results which have not been published yet since further improvements are expected.

In this paper, I consider a reduction of the 50 M Ω resistors from 52 to 8 and of the masses of all the other components by a factor of 2.

Table 3.4 compares the total activity per radioisotope in all the materials of both the detectors. From here, it becomes clear how the adjustments in the geometry and composition described in Section 2.2 and 3.2.3 make the DarkSide Low-Mass detector proposed in this research, a much more refined and pure detector, suitable for searches of DM in the low-mass range.

Total Mass of Detector Materials [kg]		
Components	DS-Proto Detector	DS-LowMass Detector
Reflector (Acrylic)	25.3	8.3
Window (Acrylic)	15.5	5.2
Cryostat (Stainless Steel)	1 233.9	0
SiPMs	370	370
LAr	345.6	345.6

Table 3.2: Full list of the masses of each of the elements that compose the detectors, except for the SiPMs for which I reported the total number of PDM units. The difference in the total mass of both the reflector panels and the windows between DS-Proto and DS-LowMass is given by the reduction in acrylic thickness from 1.5 cm to 0.5 cm. Finally the mass of StainLess steel in DS-LowMass is 0 because the cryostat was completely eliminated.

Radioactive elements Activity [$\mu\text{Bq/kg}$] or $\mu\text{Bq/PDM}$							
DS-Proto detector							
material	$^{238}\text{U}_{\text{up}}$	$^{238}\text{U}_{\text{low}}$	^{235}U	^{232}Th	$^{40}\text{K}(<)$	$^{60}\text{Co} (<)$	^{39}Ar
Acrylic	3.7	3.7	-	5.3	2592	-	0
StainLess Steel (SS)	2400	400	430	800	1200	600	0
SiPMs	1337.2	392.8	50	310.9	906.6	51.4	0
LAr	0	0	0	0	0	0	730
DS-LowMass detector							
Acrylic	3.7	3.7	-	5.3	2592	-	0
StainLess Steel (SS)	2400	400	430	800	1200	600	0
SiPMs	568.2	171.3	19.7	139.9	355.4	21.7	0
LAr	0	0	0	0	0	0	7.3

Table 3.3: Full list of the activities of each of the radioisotopes simulated in each of the materials that compose the detectors. The activity is reported as $\mu\text{Bq/kg}$ except for the SiPMs, whose activity is given in μBq per PDM. The datas are taken from the DarkSide material database which can be found at [\[1\]](#)

Total Radioactive elements Activity [mBq]							
DS-Proto detector							
material	$^{238}\text{U}_{\text{up}}$	$^{238}\text{U}_{\text{low}}$	^{235}U	^{232}Th	$^{40}\text{K} (<)$	$^{60}\text{Co} (<)$	^{39}Ar
Acrylic (Refl)	0.094	0.094	-	0.13	65.67	-	0
Acrylic (Wind)	0.058	0.058	-	0.082	40.21	-	0
SS (Cryo)	2961.35	493.56	530.58	987.12	1480.7	740.34	0
SiPMs	494.77	145.33	185.15	115.03	335.45	19	0
LAr	0	0	0	0	0	0	2523.2
DS-LowMass detector							
Acrylic (Refl)	0.03	0.03	-	0.04	21.62	-	0
Acrylic (Wind)	0.02	0.02	-	0.03	13.40	-	0
SiPMs	210.24	63.38	7.28	51.76	131.5	8.01	0
LAr	0	0	0	0	0	0	25.23

Table 3.4: Full list of the total activity of the radioisotopes simulated in all the components of the detector. This table serves to emphasize the differences between the DS-proto detector and DS-LowMass detector which are caused by: the reduction of the activity of ^{39}Ar in LAr; the reduction of the masses of Acrylic and of all the components of the SiPMs; the removal of the stainless steel cryostat.

Chapter 4

Results and Limit Calculation

To emphasize how each component of the detector contributes to the total background and to allow an easier comparison with previous results of the DarkSide collaboration, I applied the same method in the representation of the N_{e^-} spectra of the background sources. Specifically, I summed over the individual N_{e^-} spectra of each radioisotope in a particular component of the detector, for instance the cryostat, to obtain a single N_{e^-} spectrum which provides the total number of background events expected inside such component. The classification of the detector components is almost the same as that used for the MC simulations, specifically I consider 4 elements: cryostat; SiPMs; TPC (including both Reflector and Window); ^{39}Ar .

This classification, as previously mentioned, is very useful because it allows to clearly differentiate the contributions of the single elements to the total background N_{e^-} . To obtain such spectrum, I simply sum over the N_{e^-} spectra of the different detector components as just described.

4.1 The standard DS-Proto Detector

The N_{e^-} spectrum of the total background (Figure 4.2) shows a number of expected background events per kg of active LAr volume per day in the order of 10^{-2} . This result agrees with what obtained by the analysis of the 532.4 live-days DS-50 data as described in ref. [19]. This makes sense since the only major distinction between the DS-proto and DS-50 detector is given by the use of SiPM-based PDMs instead of the usual PMTs. The PDMs however are still a very large source of background given their impurities with a number of expected background events of the same order as those in the cryostat. Here is important to notice that the difference in active LAr volume between DS-50 and DS-proto is completely cancelled since the data are normalized per kg of fiducial LAr volume.

As shown in Figure 4.1, the largest contribution to the total background comes from ^{39}Ar . It follows the contribution of both SiPMs and cryostat which give an expected number of background events in the order of 0.5×10^{-3} . Finally, the smallest contribution comes from the acrylic TPC which is of order of magnitudes lower than what we get from ^{39}Ar in LAr.

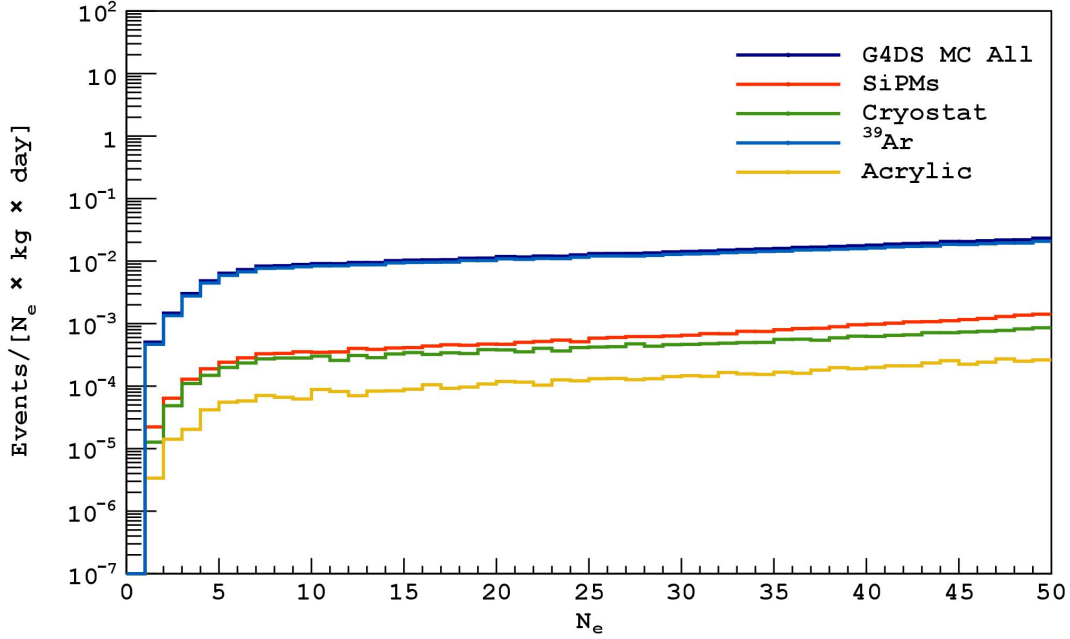


Figure 4.1: Plot of the N_{e^-} background spectrum for the DarkSide-Proto detector where on the x-axis we have the number of electron generated and on the y-axis the number of events per kg per day. The main contribution comes clearly from ^{39}Ar . It follows in order of relevance SiPMs, cryostat and acrylic. It is important to remember that the N_{e^-} background spectrum for the acrylic is simply given by the sum of the respective spectra for the reflector and windows.

4.2 The New DS-LowMass Detector

In Figure 4.2, we can clearly see how the modifications applied in the DS-LowMass detector, described fully in Section 2.2, contributed to reduce the total number of expected background events of 1 order of magnitude.

Given the removal of the cryostat and the strong reduction in the activity of ^{39}Ar in LAr, the major source of background comes from the SiPMs which give us an expected number of background events per day per kg of active LAr volume in the order of 10^{-4} .

The lowering of N_{e^-} background spectrum for the SiPMs is approximately of a factor of 2, as we would expect given the halving of the masses of all its components.

The N_{e^-} spectrum of the acrylic TPC, given the reduction in the thickness of acrylic by 1 cm, went from approximately 10^{-4} to 10^{-5} expected background events, still representing the minimum contribution to the background budget of the detector.

Overall, the reduction of the total number of background events in the DS-LowMass detector, compared to the DS-Proto detector, is of almost 2 orders of magnitude.

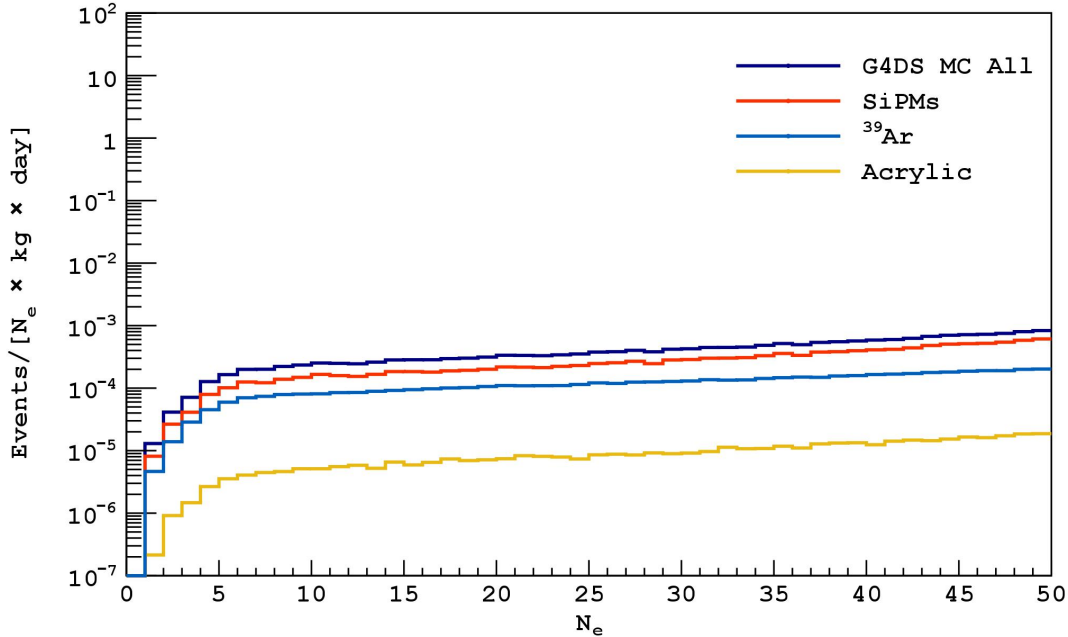


Figure 4.2: Plot of the N_{e^-} background spectrum for the DarkSide-LowMass detector. Here we can see how the strong reduction in the activity of ^{39}Ar in LAr (of 2 orders of magnitude) made the SiPMs the strongest contributor to the final N_{e^-} background spectrum. The smallest contribution still comes from the acrylic TPC which was further reduced by the reduction in the thickness of the acrylic walls by 1 cm.

4.3 Limit Calculation

The final step in this research is the computation of the Upper limits on WIMP-nucleon scattering cross-section. Generally, this would be done by comparing the data of an experiment with the expected N_{e^-} spectrum of both the total background and DM-signal, ruling out the combinations of DM mass and cross section which are incompatible. The dark matter signal is derived assuming the standard isothermal WIMP halo model, with escape velocity $v_{\text{esc}} = 544 \text{ km/s}$ [40], circular velocity $V_0 = 220 \text{ km/s}$ [40], Earth velocity $v_{\text{Earth}} = 232 \text{ km/s}$ [41], and dark matter density $0.3 \text{ GeV}/(c^2 \text{ cm}^3)$ [42].

In our case, since this is only a simulation-based research, we need to make some theoretical assumptions on the model for the expected signal. We have no a priori knowledge of the width of the ionization distribution of nuclear recoils and are not aware of measurements in liquid argon in the energy range of interest. We therefore consider, as further explained in ref. [19], an extreme model which allows for fluctuations in energy quenching, ionization yield, and recombination processes. The Upper limits on the WIMP-nucleon scattering cross-section are then extracted from the simulated N_{e^-} spectrum using a binned profile likelihood method based on a frequentist significance test as described in ref. [43, 44].

The signal region is defined using a threshold of $2e^-$, determined by the approximate end of the trapped electron background spectrum and sensitive to the entire range of DM masses explored in this work. [19]

The 90 % projected C.L. exclusion curves for DS-Proto (red-dashed line) and for DS-LowMass (black-dashed lines) are shown in Figure 4.3, in comparison with the 90 % C.L. exclusion curve from Refs. [19, 45–61], the region of claimed discovery of Refs. [62–65] and the neutrino floor for LAr experiments. [66]

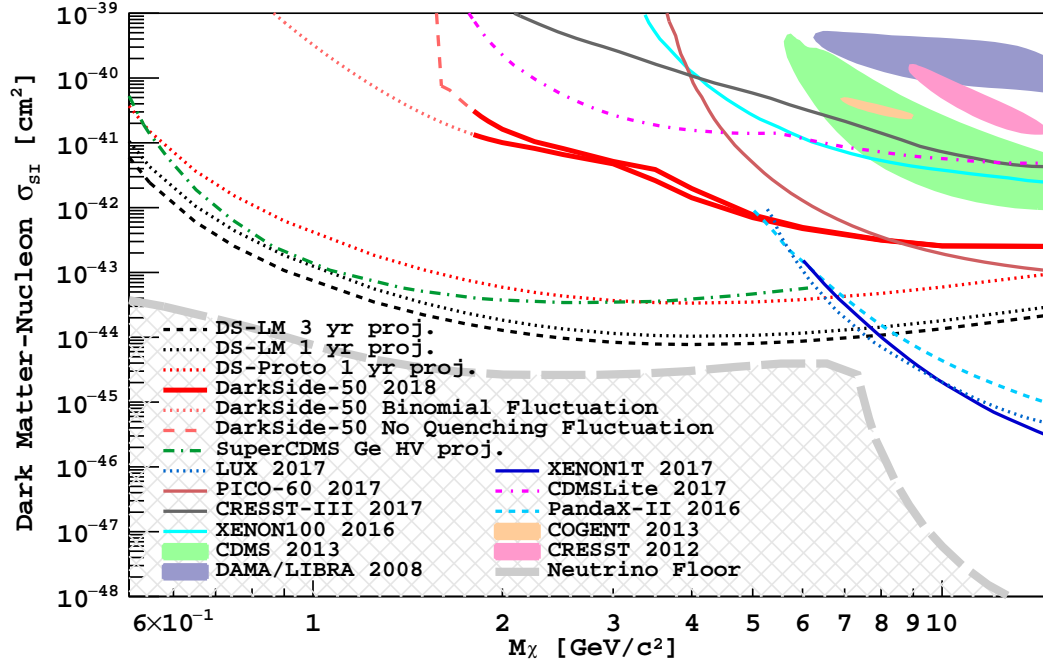



Figure 4.3: The 90 % C.L. projected exclusion curves for DS-Proto (red-dashed line) and for both 1 and 3 yr exposure DS-LowMass (black-dashed lines). The projected 3 yr exposure curve for DS-LowMass presents the world-best limit for low-mass dark matter searches in the mass range $0.6 \text{ GeV}/c^2$ to $8.0 \text{ GeV}/c^2$

The two C.L. exclusion curves of DS-LowMass represent the projection for both 1 and 3 yr exposure. ~~As we can see from the plot, an increase in the total exposure time does indeed improve the limits calculated.~~

For masses below $6.0 \text{ GeV}/c^2$, DS-Proto already presents a drastic improvement of about 2 orders of magnitude compared to the results obtained with DS-50. This difference can be explained by the increase in the target mass and the use of SiPM-based PDMs instead of standard PMTs. That said, DS-LowMass with 3 yr of exposure presents, in the same mass-range, a further improvement of almost another order of magnitude compared to the results from DS-Proto. This projected result for the DS-LowMass detector presented in this paper would represent the current world-best limit for low-mass dark matter searches in the mass range $0.6 \text{ GeV}/c^2$ to $8.0 \text{ GeV}/c^2$. 

The neutrino floor defines the point at which neutrinos, which as I described in Section 1.2.1 ~~are incredibly small and~~ interact so weakly, will start showing up as background. Comparing our results to the neutrino floor is therefore interesting because it gives us an idea of how far we are from reaching that kind of sensitivity. If on one hand hitting the floor would complicate some aspects of dark matter searches, on the other hand it would represent an incredible opportunity to study

more accurately the neutrino signals and use this information to build the next generation of dark matter detectors.

4.4 Conclusions

In this research I was able to show that, by making some adjustments to the geometry and composition of a standard detector of the DarkSide program, we can increase its sensitivity by at least one order of magnitude. The major source of background left comes from the SiPMs so they need to be the focus for the next ~~researches~~ that will aim at optimizing even further the results just shown.

The first thing to do should be to make accurate measurements on the activities of each radioisotope in all the components of the SiPMs with particular emphasis to those of , of which we are missing several data (refer to Appendix A for detailed and descriptive tables). What I expect from such measurements is a strong reduction in the total background activity in the SiPMs compared to the data available now. In fact, even if by adding more data that were lacking we should technically see an increase in the total activity of the SiPMs, accurate measurements on all the components would probably result in drastic reductions of all those many activities, of which we know only very safe upper limits (in the order of several Bq/kg).

Done that, I believe it is worth to investigate different solutions for the thickness of the acrylic walls. In fact, an increase in the thickness of acrylic could strongly reduce the amount of background events generated in the SiPMs ~~that reach~~ the active LAr volume. This consequent reduction in the expected N_{e^-} background spectrum of the SiPMs could potentially be much lower than the increase in that of the acrylic and therefore cause a further improvement in the sensitivity of the DS-LowMass detector.



Appendix A

SiPMs components Activities

The computation of the activity for each radioisotope per PDM is quite problematic. This is because SiPMs are composed by many multiple elements made in turn by different materials. As already mentioned in sec. 3.2.3, the total activity per PDM is given by summing over the activity per kg of every component of the SiPM times the mass and amount of such component in the SiPM.

The elements of a PDM are divided in two main classes: the ones that make the Front End Board (FEB) and those that compose the actual tiles.

Table A.1 shows the values of the activity of all the radioisotopes in each element of the SiPM. We immediately notice that we still lack many data for both ^{40}K and ^{60}Co and some for ^{235}U . The reason is the same as explained in sec. 3.2.3. Generally, searches for dark matter in the low-mass range are a very new area of study, thus more measurements on all the activities of these radioisotopes will definitely be made in the coming months and years, filling all the blanks in this table.

In table A.2 for each component we are given its mass and the number of such component inside one PDM. Apart from the $50\text{ M}\Omega$ resistors whose mass remain unchanged, all the other components face a reduction in their mass by a factor of 2 in the DS-LowMass detector. On the other hand, meanwhile all the other components are kept at the same amount, the number of $50\text{ M}\Omega$ resistors is reduced from 52 to 8 in the DS-LowMass detector.

The computation of the total activity per PDM for both detectors is therefore trivial and is given by summing the values in table A.1 multiplied by the respective masses and units found in table A.2

Radioisotopes Activity in every SiPM component [mBq/kg]						
component	$^{238}\text{U}^{\text{up}}$	$^{238}\text{U}^{\text{low}}$	^{235}U	^{232}Th	^{40}K (<)	^{60}Co (<)
SiPM Tiles						
Cu PCB	0.01	0.01	-	0	-	4.7
Invar	1.5	1.5	0.02	1.1	2.9	0.7
PCB adhesive	50	50	5	25	-	-
Connector	12	12	-	12	-	-
Resistor (50 M Ω)	4000	1000	220	620	3900	160
Capacitor (large)	270	300	-	200	2800	73
Solder	1.1	14000	-	2.1	-	-
Clips for housing	3	3	-	1	-	-
Glass	3900	3900	-	850	-	-
Front End Board (FEB)						
Cu PCB	0.01	0.01	-	0	-	4.7
PCB adhesive	50	50	5	25	-	-
connectors tile	3.6	3.6	-	3.2	-	-
connector to fingers	3.6	3.6	-	3.2	-	-
Op. Amp LMH6629	85	85	-	12	560	15
Sum Amp. OPA838	85	85	-	12	560	15
Diff. Amp. THS4522	85	85	-	12	560	15
Resistor	8100	7000	600	3600	-	-
Panasonic PPS caps	49	49	-	10	-	-
Solder	1.1	14000	-	2.1	-	-
diode	0	0	0	0	0	0
AVR microcontroller	85	85	-	12	560	15
Acrylic housing	21	0.91	0	1.2	-	-
mushrooms	0.33	0.33	-	0.02	-	-
Circlip (seeger)	2.4	0.4	0.1	0.8	2.5	13

Table A.1: Mass and units of each component of the SiPMs for the two detectors considered in this research. The elements are divided in two categories: those composing the actual tiles and those making the FEB.

Mass and Number of SiPMs Components				
component	DS-Proto Detector		DS-LowMass Detector	
	mass	number	mass	number
SiPM Tiles	[m kg]		[m kg]	
Cu PCB	1600	1	800	1
Invar	10125	1	5063	1
PCB adhesive	250	1	125	1
Connector	87.5	2	43.8	2
Resistor (50 M Ω)	2	52	2	8
Capacitor (large)	10	4	5	4
Solder	1000	1	500	1
Clips for housing	43	4	21.5	4
Glass	1150	1	575	1
Front End Board (FEB)				
Cu PCB	1700	1	850	1
PCB adhesive	250	1	125	1
connectors tile	60	2	30	2
connector to fingers	80	1	40	1
Op. Amp LMH6629	10	4	5	4
Sum Amp. OPA838	20	1	10	1
Diff. Amp. THS4522	20	1	10	1
Resistor	0.6	70	0.3	70
Panasonic PPS caps	9	20	4.5	20
Solder	1000	1	500	1
diode	30	1	15	1
AVR microcontroller	500	1	250	1
Acrylic housing	18000	1	9000	1
mushrooms	3500	2	1750	2
Circlip (seeger)	125	4	62.5	4

Table A.2: Radioisotopes activity in every SiPM component as found in the DarkSide materials database [1]. As we can clearly observe many data are missing or are only limits on the actual activities which if accurately measured will probably result to be much lower than shown.

Bibliography

- [1] “Darkside materials database.” [Online]. Available: <http://darkside.if.uj.edu.pl/>
- [2] “Super symmetric dark matter.” [Online]. Available: <https://arxiv.org/pdf/hep-ph/9506380.pdf>
- [3] “Galaxy cluster abell.” [Online]. Available: http://hubblesite.org/about_us/copyright.php
- [4] D. Clowe, A. H. Gonzalez, M. Markevitch, S. W. Randall, C. Jones, and D. Zaritsky, “A direct empirical proof of the existence of dark matter,” *The Astrophysical Journal Letters*, vol. 648, no. 2, p. L109, 2006. [Online]. Available: <http://stacks.iop.org/1538-4357/648/i=2/a=L109>
- [5] “The history of dark matter.” [Online]. Available: <https://arxiv.org/abs/1605.04909>
- [6] V. C. Rubin, N. Thonnard, and W. K. Ford, Jr., “Extended rotation curves of high-luminosity spiral galaxies. IV - systematic dynamical properties, SA through SC,” *Astrophysical Journal, Part 2 - Letters to the Editor*, vol. 225, pp. L107–L111, 1978.
- [7] “Cmb.” [Online]. Available: <https://map.gsfc.nasa.gov/media/121238/index.html>
- [8] K. Freeman and G. McNamara, *In Search of Dark Matter*, ser. Springer Praxis Books. Springer New York, 2006. [Online]. Available: <https://books.google.com/books?id=C2OS1kmQ8JIC>
- [9] G. Bertone, *Particle Dark Matter: Observations, Models and Searches*. Cambridge University Press, 2010. [Online]. Available: <https://books.google.com/books?id=JkUgAwAAQBAJ>
- [10] E. Kolb, *The Early Universe*. CRC Press, 2018. [Online]. Available: <https://books.google.com/books?id=FwpQDwAAQBAJ>
- [11] *Cosmology*. [Online]. Available: <http://www.damtp.cam.ac.uk/user/db275/Cosmology/Chapter3.pdf>
- [12] “Big bang nucleosynthesis.” [Online]. Available: https://en.wikipedia.org/wiki/Big_Bang_nucleosynthesis
- [13] F. Kahlhoefer, “Review of lhc dark matter searches,” *International Journal of Modern Physics A*, vol. 32, no. 13, p. 1730006, 2017. [Online]. Available: <https://doi.org/10.1142/S0217751X1730006X>

-
- [14] J. M. Gaskins, “A review of indirect searches for particle dark matter,” *Contemporary Physics*, vol. 57, no. 4, pp. 496–525, 2016. [Online]. Available: <https://doi.org/10.1080/00107514.2016.1175160>
- [15] T. D. Collaboration, “The darkside program.” [Online]. Available: https://www.epj-conferences.org/articles/epjconf/pdf/2016/16/epjconf-RICAP-14_06010.pdf
- [16] P. Agnes, T. Alexander, A. Alton, K. Arisaka, H. Back, B. Baldin, K. Biery, G. Bonfini, M. Bossa, A. Brigatti, J. Brodsky, F. Budano, L. Cadonati, F. Calaprice, N. Canci, A. Candela, H. Cao, M. Cariello, P. Cavalcante, A. Chavarria, A. Chepurnov, A. Cocco, L. Crippa, D. D’Angelo, M. D’Incecco, S. Davini, M. D. Deo, A. Derbin, A. Devoto, F. D. Eusanio, G. D. Pietro, E. Edkins, A. Empl, A. Fan, G. Fiorillo, K. Fomenko, G. Forster, D. Franco, F. Gabriele, C. Galbiati, A. Goretti, L. Grandi, M. Gromov, M. Guan, Y. Guardincerri, B. Hackett, K. Herner, E. Hungerford, A. Ianni, A. Ianni, C. Jollet, K. Keeter, C. Kendziora, S. Kidner, V. Kobychiev, G. Koh, D. Korablev, G. Korga, A. Kurlej, P. Li, B. Loer, P. Lombardi, C. Love, L. Ludhova, S. Luitz, Y. Ma, I. Machulin, A. Mandarano, S. Mari, J. Maricic, L. Marini, C. Martoff, A. Meregaglia, E. Meroni, P. Meyers, R. Milincic, D. Montanari, A. Monte, M. Montuschi, M. Monzani, P. Mosteiro, B. Mount, V. Muratova, P. Musico, A. Nelson, S. Odrowski, M. Okounkova, M. Orsini, F. Ortica, L. Pagani, M. Pallavicini, E. Pantic, L. Papp, S. Parmeggiano, R. Parsells, K. Pelczar, N. Pelliccia, S. Perasso, A. Pocar, S. Pordes, D. Pugachev, H. Qian, K. Randle, G. Ranucci, A. Razeto, B. Reinhold, A. Renshaw, A. Romani, B. Rossi, N. Rossi, S. Rountree, D. Sablone, P. Saggese, R. Saldanha, W. Sands, S. Sangiorgio, E. Segreto, D. Semenov, E. Shields, M. Skorokhvatov, O. Smirnov, A. Sotnikov, C. Stanford, Y. Suvorov, R. Tartaglia, J. Tatarowicz, G. Testera, A. Tonazzo, E. Unzhakov, R. Vogelaar, M. Wada, S. Walker, H. Wang, Y. Wang, A. Watson, S. Westerdale, M. Wojcik, A. Wright, X. Xiang, J. Xu, C. Yang, J. Yoo, S. Zavatarelli, A. Zec, C. Zhu, and G. Zuzel, “First results from the darkside-50 dark matter experiment at laboratori nazionali del gran sasso,” *Physics Letters B*, vol. 743, pp. 456 – 466, 2015. [Online]. Available: <http://www.sciencedirect.com/science/article/pii/S0370269315001756>
- [17] C. E. Aalseth *et al.*, “DarkSide-20k: A 20 tonne two-phase LAr TPC for direct dark matter detection at LNGS,” *Eur. Phys. J. Plus*, vol. 133, p. 131, 2018.
- [18] “An introduction to the silicon photomultiplier by sensl.” [Online]. Available: <https://www.sensl.com/downloads/ds/TN%20-%20Intro%20to%20SPM%20Tech.pdf>
- [19] P. Agnes, I. F. M. Albuquerque, T. Alexander, A. K. Alton, G. R. Araujo, D. M. Asner, M. Ave, H. O. Back, B. Baldin, G. Batignani, K. Biery, V. Bocci, G. Bonfini, W. Bonivento, B. Bottino, F. Budano, S. Bussino, M. Cadeddu, M. Cadoni, F. Calaprice, A. Caminata, N. Canci, A. Candela, M. Caravati, M. Cariello, M. Carlini, M. Carpinelli, S. Catalanotti, V. Cataudella, P. Cavalcante, S. Caviuoti, R. Cereseto, A. Chepurnov, C. Cicalò, L. Cifarelli, A. G. Cocco, G. Covone, D. D’Angelo, M. D’Incecco, D. D’Urso, S. Davini, A. De Candia,

-
- S. De Cecco, M. De Deo, G. De Filippis, G. De Rosa, M. De Vincenzi, P. Demontis, A. V. Derbin, A. Devoto, F. Di Eusano, G. Di Pietro, C. Dionisi, M. Downing, E. Edkins, A. Empl, A. Fan, G. Fiorillo, K. Fomenko, D. Franco, F. Gabriele, A. Gabrieli, C. Galbiati, P. Garcia Abia, C. Ghiano, S. Giagu, C. Giganti, G. K. Giovanetti, O. Gorchakov, A. M. Goretti, F. Granato, M. Gromov, M. Guan, Y. Guardincerri, M. Gulino, B. R. Hackett, M. H. Hassanshahi, K. Herner, B. Hosseini, D. Hughes, P. Humble, E. V. Hungerford, A. Ianni, A. Ianni, V. Ippolito, I. James, T. N. Johnson, Y. Kahn, K. Keeter, C. L. Kendziora, I. Kochanek, G. Koh, D. Korablev, G. Korga, A. Kubankin, M. Kuss, M. La Commara, M. Lai, X. Li, M. Lisanti, M. Lissia, B. Loer, G. Longo, Y. Ma, A. A. Machado, I. N. Machulin, A. Mandarano, L. Mapelli, S. M. Mari, J. Maricic, C. J. Martoff, A. Messina, P. D. Meyers, R. Milincic, S. Mishra-Sharma, A. Monte, M. Morrocchi, B. J. Mount, V. N. Muratova, P. Musico, R. Nania, A. Navrer Agasson, A. O. Nozdrina, A. Oleinik, M. Orsini, F. Ortica, L. Pagani, M. Pallavicini, L. Pandola, E. Pantic, E. Paoloni, F. Pazzona, K. Pelczar, N. Pelliccia, V. Pesudo, A. Pocar, S. Pordes, S. S. Poudel, D. A. Pugachev, H. Qian, F. Ragusa, M. Razeti, A. Razeto, B. Reinhold, A. L. Renshaw, M. Rescigno, Q. Riffard, A. Romani, B. Rossi, N. Rossi, D. Sablone, O. Samoylov, W. Sands, S. Sanfilippo, M. Sant, R. Santorelli, C. Savarese, E. Scapparone, B. Schlitzer, E. Segreto, D. A. Semenov, A. Shchagin, A. Sheshukov, P. N. Singh, M. D. Skorokhvatov, O. Smirnov, A. Sotnikov, C. Stanford, S. Stracka, G. B. Suffritti, Y. Suvorov, R. Tartaglia, G. Testera, A. Tonazzo, P. Trinchese, E. V. Unzhakov, M. Verducci, A. Vishneva, B. Vogelaar, M. Wada, T. J. Waldrop, H. Wang, Y. Wang, A. W. Watson, S. Westerdale, M. M. Wojcik, M. Wojcik, X. Xiang, X. Xiao, C. Yang, Z. Ye, C. Zhu, A. Zichichi, and G. Zuzel, “Low-mass dark matter search with the darkside-50 experiment,” *Phys. Rev. Lett.*, vol. 121, p. 081307, Aug 2018. [Online]. Available: <https://link.aps.org/doi/10.1103/PhysRevLett.121.081307>
- [20] J. Alexander *et al.*, “Dark sectors 2016 workshop: Community report,” 2016. [Online]. Available: <http://lss.fnal.gov/archive/2016/conf/fermilab-conf-16-421.pdf>
- [21] the DarkSide Collaboration, “Report to the xlx lngs scientific committee, the darkside collaboration.”
- [22] H. O. Back *et al.*, “First large scale production of low radioactivity argon from underground sources,” 2012.
- [23] P. Agnes, L. Agostino, I. Albuquerque, T. Alexander, A. Alton, K. Arisaka, H. Back, B. Baldin, K. Biery, G. Bonfini, M. Bossa, B. Bottino, A. Brigatti, J. Brodsky, F. Budano, S. Bussino, M. Cadeddu, L. Cadonati, M. Cadoni, F. Calaprice, N. Canci, A. Candela, H. Cao, M. Cariello, M. Carlini, S. Catalanotti, P. Cavalcante, A. Chepurnov, A. Cocco, G. Covone, L. Crippa, D. D’Angelo, M. D’Incecco, S. Davini, S. D. Cecco, M. D. Deo, M. D. Vincenzi, A. Derbin, A. Devoto, F. D. Eusano, G. D. Pietro, E. Edkins, A. Empl, A. Fan, G. Fiorillo, K. Fomenko, G. Foster, D. Franco, F. Gabriele, C. Galbiati, C. Giganti, A. Goretti, F. Granato, L. Grandi, M. Gromov, M. Guan, Y. Guardincerri, B. Hackett,

-
- K. Herner, E. Hungerford, A. Ianni, A. Ianni, I. James, T. Johnson, C. Jollet, K. Keeter, C. Kendziora, V. Kobychiev, G. Koh, D. Korablev, G. Korga, A. Kubankin, X. Li, M. Lissia, P. Lombardi, S. Luitz, Y. Ma, I. Machulin, A. Mandarano, S. Mari, J. Maricic, L. Marini, C. Martoff, A. Mereaglia, P. Meyers, T. Miletic, R. Milincic, D. Montanari, A. Monte, M. Montuschi, M. Monzani, P. Mosteiro, B. Mount, V. Muratova, P. Musico, J. Napolitano, A. Nelson, S. Odrowski, M. Orsini, F. Ortica, L. Pagani, M. Pallavicini, E. Pantic, S. Parmeggiano, K. Pelczar, N. Pelliccia, S. Perasso, A. Pocar, S. Pordes, D. Pugachev, H. Qian, K. Randle, G. Ranucci, A. Razeto, B. Reinhold, A. Renshaw, A. Romani, B. Rossi, N. Rossi, S. Rountree, D. Sablone, P. Saggese, R. Saldanha, W. Sands, S. Sangiorgio, C. Savarese, E. Segreto, D. Semenov, E. Shields, P. Singh, M. Skorokhvatov, O. Smirnov, A. Sotnikov, C. Stanford, Y. Suvorov, R. Tartaglia, J. Tatarowicz, G. Testera, A. Tonazzo, P. Trinchese, E. Unzhakov, A. Vishneva, R. Vogelaar, M. Wada, S. Walker, H. Wang, Y. Wang, A. Watson, S. Westerdale, J. Wilhelmi, M. Wojcik, X. Xiang, J. Xu, C. Yang, J. Yoo, S. Zavatarelli, A. Zec, W. Zhong, C. Zhu, and G. Zuzel, “The veto system of the darkside-50 experiment,” *Journal of Instrumentation*, vol. 11, no. 03, p. P03016, 2016. [Online]. Available: <http://stacks.iop.org/1748-0221/11/i=03/a=P03016>
- [24] C. Savarese, “A novel light detector for darkside-20k,” *Ph.D. thesis, Gran Sasso Science Institute (2017)*.
- [25] S. S. Westerdale, “A study of nuclear recoil backgrounds in dark matter detectors,” *Ph.D. thesis, Princeton University (2016)*.
- [26] M. Z. M. J. Berger, J. Coursey and J. Chang, “Stopping-power and range tables for electrons, protons, and helium ions.” [Online]. Available: <https://www.nist.gov/pml/stopping-power-range-tables-electrons-protons-and-helium-ions>
- [27] S. H. A. Koning and S. Goriely, *Talys-1.6, Nuclear Reaction Program*, 2013. [Online]. Available: <http://www.talys.eu/fileadmin/talys/user/docs/talys1.6.pdf>
- [28] N. N. D. Center, “Information extracted from the chart of nuclides database (2018).” [Online]. Available: <https://www.nndc.bnl.gov/>
- [29] C. Stanford, “Alphas and surface backgrounds in liquid argon dark matter detectors,” *Ph.D. thesis, Princeton University (2017)*.
- [30] W. Maneschg, M. Laubenstein, W. Hampel, G. Heusser, B. Schwingenheuer, and H. Simgen, “Measurements of extremely low radioactivity levels in stainless steel for gerda,” *Nuclear Instruments and Methods in Physics Research Section A: Accelerators, Spectrometers, Detectors and Associated Equipment*, vol. 593, no. 3, pp. 448 – 453, 2008. [Online]. Available: <http://www.sciencedirect.com/science/article/pii/S0168900208007833>
- [31] G. Koh, “A dark matter search with darkside-50,” *Ph.D. thesis, Princeton University (2018)*.

-
- [32] “Monte carlo method.” [Online]. Available: https://en.wikipedia.org/wiki/Monte_Carlo_method
- [33] P. Agnes, I. Albuquerque, T. Alexander, A. Alton, D. Asner, H. Back, K. Biery, V. Bocci, G. Bonfini, W. Bonivento, M. Bossa, B. Bottino, F. Budano, S. Bussino, M. Cadeddu, M. Cadoni, F. Calaprice, N. Canci, A. Candela, M. Caravati, M. Cariello, M. Carlini, S. Catalanotti, V. Cataudella, P. Cavalcante, A. Chepurnov, C. Cicala, A. Cocco, G. Covone, D. D’Angelo, M. D’Incecco, S. Davini, A. de Candia, S. D. Cecco, M. D. Deo, G. D. Filippis, M. D. Vincenzi, A. Derbin, G. D. Rosa, A. Devoto, F. D. Eusanio, G. D. Pietro, C. Dionisi, E. Edkins, A. Empl, A. Fan, G. Fiorillo, K. Fomenko, D. Franco, F. Gabriele, C. Galbiati, S. Giagu, C. Giganti, G. Giovanetti, A. Goretti, F. Granato, M. Gromov, M. Guan, Y. Guardincerri, B. Hackett, K. Herner, D. Hughes, P. Humble, E. Hungerford, A. Ianni, I. James, T. Johnson, K. Keeter, C. Kendziora, G. Koh, D. Korablev, G. Korga, A. Kubankin, X. Li, M. Lissia, B. Loer, G. Longo, Y. Ma, A. Machado, I. Machulin, A. Mandarano, S. Mari, J. Maricic, C. Martoff, P. Meyers, R. Milincic, A. Monte, B. Mount, V. Muratova, P. Musico, J. Napolitano, A. N. Agasson, A. Oleinik, M. Orsini, F. Ortica, L. Pagani, M. Pallavicini, E. Pantic, K. Pelczar, N. Pelliccia, A. Pocar, S. Pordes, D. A. Pugachev, H. Qian, K. Randle, M. Razeti, A. Razeto, B. Reinhold, A. Renshaw, M. Rescigno, Q. Riffard, A. Romani, B. Rossi, N. Rossi, D. Sablone, W. Sands, S. Sanfilippo, C. Savarese, B. Schlitzer, E. Segreto, D. A. Semenov, P. Singh, M. Skorokhvatov, O. Smirnov, A. Sotnikov, C. Stanford, Y. Suvorov, R. Tartaglia, G. Testera, A. Tonazzo, P. Trinchese, E. Unzhakov, M. Verducci, A. Vishneva, B. Vogelaar, M. Wada, S. Walker, H. Wang, Y. Wang, A. Watson, S. Westerdale, J. Wilhelmi, M. Wojcik, X. Xiang, X. Xiao, C. Yang, Z. Ye, C. Zhu, and G. Zuzel, “Simulation of argon response and light detection in the darkside-50 dual phase tpc,” *Journal of Instrumentation*, vol. 12, no. 10, p. P10015, 2017. [Online]. Available: <http://stacks.iop.org/1748-0221/12/i=10/a=P10015>
- [34] S. Kubota, A. Nakamoto, T. Takahashi, S. Konno, T. Hamada, M. Miyajima, A. Hitachi, E. Shibamura, and T. Doke, “Evidence of the existence of excitation states in liquid argon and exciton-enhanced ionization from xenon doping,” *Phys. Rev. B*, vol. 13, pp. 1649–1653, Feb 1976. [Online]. Available: <https://link.aps.org/doi/10.1103/PhysRevB.13.1649>
- [35] T. Doke, A. Hitachi, J. Kikuchi, K. Masuda, H. Okada, and E. Shibamura, “Absolute scintillation yields in liquid argon and xenon for various particles,” *Japanese Journal of Applied Physics*, vol. 41, no. 3R, p. 1538, 2002. [Online]. Available: <http://stacks.iop.org/1347-4065/41/i=3R/a=1538>
- [36] J. Thomas and D. A. Imel, “Recombination of electron-ion pairs in liquid argon and liquid xenon,” *Phys. Rev. A*, vol. 36, pp. 614–616, Jul 1987. [Online]. Available: <https://link.aps.org/doi/10.1103/PhysRevA.36.614>
- [37] P. Agnes, I. F. M. Albuquerque, T. Alexander, A. K. Alton, G. R. Araujo, D. M. Asner, M. Ave, H. O. Back, B. Baldin, G. Batignani, K. Biery, V. Bocci, G. Bonfini,

-
- W. Bonivento, B. Bottino, F. Budano, S. Bussino, M. Cadeddu, M. Cadoni, F. Calaprice, A. Caminata, N. Canci, A. Candela, M. Caravati, M. Cariello, M. Carlini, M. Carpinelli, S. Catalanotti, V. Cataudella, P. Cavalcante, S. Caviuoti, R. Cereseto, A. Chepurnov, C. Cicalò, L. Cifarelli, A. G. Cocco, G. Covone, D. D'Angelo, M. D'Incecco, D. D'Urso, S. Davini, A. De Candia, S. De Cecco, M. De Deo, G. De Filippis, G. De Rosa, M. De Vincenzi, P. Demontis, A. V. Derbin, A. Devoto, F. Di Eusanio, G. Di Pietro, C. Dionisi, M. Downing, E. Edkins, A. Empl, A. Fan, G. Fiorillo, K. Fomenko, D. Franco, F. Gabriele, A. Gabrieli, C. Galbiati, P. Garcia Abia, C. Ghiano, S. Giagu, C. Giganti, G. K. Giovanetti, O. Gorchakov, A. M. Goretti, F. Granato, M. Gromov, M. Guan, Y. Guardincerri, M. Gulino, B. R. Hackett, M. H. Hassanshahi, K. Herner, B. Hosseini, D. Hughes, P. Humble, E. V. Hungerford, A. Ianni, A. Ianni, V. Ippolito, I. James, T. N. Johnson, Y. Kahn, K. Keeter, C. L. Kendziora, I. Kochanek, G. Koh, D. Korablev, G. Korga, A. Kubankin, M. Kuss, M. La Commara, M. Lai, X. Li, M. Lisanti, M. Lissia, B. Loer, G. Longo, Y. Ma, A. A. Machado, I. N. Machulin, A. Mandarano, L. Mapelli, S. M. Mari, J. Maricic, C. J. Martoff, A. Messina, P. D. Meyers, R. Milincic, S. Mishra-Sharma, A. Monte, M. Morrocchi, B. J. Mount, V. N. Muratova, P. Musico, R. Nania, A. Navrer Agasson, A. O. Nozdrina, A. Oleinik, M. Orsini, F. Ortica, L. Pagani, M. Pallavicini, L. Pandola, E. Pantic, E. Paoloni, F. Pazzona, K. Pelczar, N. Pelliccia, V. Pesudo, E. Picciau, A. Pocar, S. Pordes, S. S. Poudel, D. A. Pugachev, H. Qian, F. Ragusa, M. Razeti, A. Razeto, B. Reinhold, A. L. Renshaw, M. Rescigno, Q. Riffard, A. Romani, B. Rossi, N. Rossi, D. Sablone, O. Samoylov, W. Sands, S. Sanfilippo, M. Sant, R. Santorelli, C. Savarese, E. Scapparone, B. Schlitzer, E. Segreto, D. A. Semenov, A. Shchagin, A. Sheshukov, P. N. Singh, M. D. Skorokhvatov, O. Smirnov, A. Sotnikov, C. Stanford, S. Stracka, G. B. Suffritti, Y. Suvorov, R. Tartaglia, G. Testera, A. Tonazzo, P. Trinchese, E. V. Unzhakov, M. Verducci, A. Vishneva, B. Vogelaar, M. Wada, T. J. Waldrop, H. Wang, Y. Wang, A. W. Watson, S. Westerdale, M. M. Wojcik, M. Wojcik, X. Xiang, X. Xiao, C. Yang, Z. Ye, C. Zhu, A. Zichichi, and G. Zuzel, "Constraints on sub-gev dark-matter electron scattering from the darkside-50 experiment," *Phys. Rev. Lett.*, vol. 121, p. 111303, Sep 2018. [Online]. Available: <https://link.aps.org/doi/10.1103/PhysRevLett.121.111303>
- [38] X.-Y. Li, Z.-Y. Deng, L.-J. Wen, W.-D. Li, Z.-Y. You, C.-X. Yu, Y.-M. Zhang, and T. Lin, "Simulation of natural radioactivity backgrounds in the juno central detector," *Chinese Physics C*, vol. 40, no. 2, p. 026001, 2016. [Online]. Available: <http://stacks.iop.org/1674-1137/40/i=2/a=026001>
- [39] "A 350-metre-tall tower to purify argon." [Online]. Available: <https://home.cern/news/news/engineering/350-metre-tall-tower-purify-argon>
- [40] G. C. Hanna, D. H. W. Kirkwood, and B. Pontecorvo, "High multiplication proportional counters for energy measurements," *Phys. Rev.*, vol. 75, pp. 985–986, Mar 1949. [Online]. Available: <https://link.aps.org/doi/10.1103/PhysRev.75.985.2>

-
- [41] B. R. Joshi, “Orbital electron capture ratio and beta spectrum of ^{204}Tl ,” *Proceedings of the Physical Society*, vol. 77, no. 6, p. 1205, 1961. [Online]. Available: <http://stacks.iop.org/0370-1328/77/i=6/a=315>
- [42] R. Firestone, C. Baglin, and S. Chu, *Table of Isotopes: 1999 Update*, ser. A Wiley-Interscience publication. Wiley, 1999, no. v. 4. [Online]. Available: <https://books.google.com/books?id=W4JUAAAAMAAJ>
- [43] G. Cowan, K. Cranmer, E. Gross, and O. Vitells, “Asymptotic formulae for likelihood-based tests of new physics,” *The European Physical Journal C*, vol. 71, no. 2, p. 1554, Feb 2011. [Online]. Available: <https://doi.org/10.1140/epjc/s10052-011-1554-0>
- [44] W. VERKERKE and D. KIRKBY, *THE ROOFIT TOOLKIT FOR DATA MODELING*, pp. 186–189. [Online]. Available: https://www.worldscientific.com/doi/abs/10.1142/9781860948985_0039
- [45] E. Aprile, J. Aalbers, F. Agostini, M. Alfonsi, F. D. Amaro, M. Anthony, F. Arneodo, P. Barrow, L. Baudis, B. Bauermeister, M. L. Benabderrahmane, T. Berger, P. A. Breur, A. Brown, E. Brown, S. Bruenner, G. Bruno, R. Budnik, A. Buss, L. Bütikofer, J. M. R. Cardoso, M. Cervantes, D. Cichon, D. Coderre, A. P. Colijn, J. Conrad, J. P. Cussonneau, M. P. Decowski, P. de Perio, P. Di Gangi, A. Di Giovanni, E. Duchovni, A. D. Ferella, A. Fieguth, D. Franco, W. Fulgione, M. Galloway, M. Garbini, C. Geis, L. W. Goetzke, Z. Greene, C. Grignon, E. Gross, C. Hasterok, E. Hogenbirk, R. Itay, B. Kaminsky, G. Kessler, A. Kish, H. Landsman, R. F. Lang, L. Levinson, M. Le Calloch, C. Levy, F. Linde, S. Lindemann, M. Lindner, J. A. M. Lopes, A. Lyashenko, A. Manfredini, T. Marrodán Undagoitia, J. Masbou, F. V. Massoli, D. Masson, D. Mayani, A. J. Melgarejo Fernandez, Y. Meng, M. Messina, K. Micheneau, B. Miguez, A. Molinario, M. Murra, J. Naganoma, U. Oberlack, S. E. A. Orrigo, P. Pakarha, B. Pelssers, R. Persiani, F. Piastra, J. Pienaar, G. Plante, N. Priel, L. Rauch, S. Reichard, C. Reuter, A. Rizzo, S. Rosendahl, N. Rupp, J. M. F. dos Santos, G. Sartorelli, M. Scheibelhut, S. Schindler, J. Schreiner, M. Schumann, L. Scotto Lavina, M. Selvi, P. Shagin, H. Simgen, A. Stein, D. Thers, A. Tiseni, G. Trincherro, C. D. Tunnell, M. von Sivers, R. Wall, H. Wang, M. Weber, Y. Wei, C. Weinheimer, J. Wulf, and Y. Zhang, “Low-mass dark matter search using ionization signals in xenon100,” *Phys. Rev. D*, vol. 94, p. 092001, Nov 2016. [Online]. Available: <https://link.aps.org/doi/10.1103/PhysRevD.94.092001>
- [46] R. Agnese, A. J. Anderson, M. Asai, D. Balakishiyeva, R. Basu Thakur, D. A. Bauer, J. Billard, A. Borgland, M. A. Bowles, D. Brandt, P. L. Brink, R. Bunker, B. Cabrera, D. O. Caldwell, D. G. Cerdeno, H. Chagani, J. Cooley, B. Cornell, C. H. Crewdson, P. Cushman, M. Daal, P. C. F. Di Stefano, T. Doughty, L. Esteban, S. Fallows, E. Figueroa-Feliciano, G. L. Godfrey, S. R. Golwala, J. Hall, H. R. Harris, S. A. Hertel, T. Hofer, D. Holmgren, L. Hsu, M. E. Huber, A. Jastram, O. Kamaev, B. Kara, M. H. Kelsey, A. Kennedy,

-
- M. Kiveni, K. Koch, B. Loer, E. Lopez Asamar, R. Mahapatra, V. Mandic, C. Martinez, K. A. McCarthy, N. Mirabolfathi, R. A. Moffatt, D. C. Moore, P. Nadeau, R. H. Nelson, K. Page, R. Partridge, M. Pepin, A. Phipps, K. Prasad, M. Pyle, H. Qiu, W. Rau, P. Redl, A. Reisetter, Y. Ricci, T. Saab, B. Sadoulet, J. Sander, K. Schneck, R. W. Schnee, S. Scorza, B. Serfass, B. Shank, D. Speller, A. N. Villano, B. Welliver, D. H. Wright, S. Yellin, J. J. Yen, B. A. Young, and J. Zhang, “Search for low-mass weakly interacting massive particles using voltage-assisted calorimetric ionization detection in the supercdms experiment,” *Phys. Rev. Lett.*, vol. 112, p. 041302, Jan 2014. [Online]. Available: <https://link.aps.org/doi/10.1103/PhysRevLett.112.041302>
- [47] R. Agnese, A. J. Anderson, M. Asai, D. Balakishiyeva, R. Basu Thakur, D. A. Bauer, J. Beaty, J. Billard, A. Borgland, M. A. Bowles, D. Brandt, P. L. Brink, R. Bunker, B. Cabrera, D. O. Caldwell, D. G. Cerdeno, H. Chagani, Y. Chen, M. Cherry, J. Cooley, B. Cornell, C. H. Crewdson, P. Cushman, M. Daal, D. DeVaney, P. C. F. Di Stefano, E. D. C. E. Silva, T. Doughty, L. Esteban, S. Fallows, E. Figueroa-Feliciano, G. L. Godfrey, S. R. Golwala, J. Hall, S. Hansen, H. R. Harris, S. A. Hertel, B. A. Hines, T. Hofer, D. Holmgren, L. Hsu, M. E. Huber, A. Jastram, O. Kamaev, B. Kara, M. H. Kelsey, S. Kenany, A. Kennedy, M. Kiveni, K. Koch, A. Leder, B. Loer, E. Lopez Asamar, R. Mahapatra, V. Mandic, C. Martinez, K. A. McCarthy, N. Mirabolfathi, R. A. Moffatt, R. H. Nelson, L. Novak, K. Page, R. Partridge, M. Pepin, A. Phipps, M. Platt, K. Prasad, M. Pyle, H. Qiu, W. Rau, P. Redl, A. Reisetter, R. W. Resch, Y. Ricci, M. Ruschman, T. Saab, B. Sadoulet, J. Sander, R. L. Schmitt, K. Schneck, R. W. Schnee, S. Scorza, D. N. Seitz, B. Serfass, B. Shank, D. Speller, A. Tomada, S. Upadhyayula, A. N. Villano, B. Welliver, D. H. Wright, S. Yellin, J. J. Yen, B. A. Young, and J. Zhang, “Search for low-mass weakly interacting massive particles with supercdms,” *Phys. Rev. Lett.*, vol. 112, p. 241302, Jun 2014. [Online]. Available: <https://link.aps.org/doi/10.1103/PhysRevLett.112.241302>
- [48] G. Angloher, A. Bento, C. Bucci, L. Canonica, X. Defay, A. Erb, F. von Feilitzsch, N. F. Iachellini, P. Gorla, A. Gütlein, D. Hauff, J. Jochum, M. Kiefer, H. Kluck, H. Kraus, J. C. Lanfranchi, J. Loebell, A. Münster, C. Pagliarone, F. Petricca, W. Potzel, F. Pröbst, F. Reindl, K. Schäffner, J. Schieck, S. Schönert, W. Seidel, L. Stodolsky, C. Strandhagen, R. Strauss, A. Tanzke, H. H. Trinh Thi, C. Türkoğlu, M. Uffinger, A. Ulrich, I. Usherov, S. Wawoczny, M. Willers, M. Wüstrich, and A. Zöller, “Results on light dark matter particles with a low-threshold cress-tii detector,” *The European Physical Journal C*, vol. 76, no. 1, p. 25, Jan 2016. [Online]. Available: <https://doi.org/10.1140/epjc/s10052-016-3877-3>
- [49] W. Zhao, Q. Yue, K. J. Kang, J. P. Cheng, Y. J. Li, H. T. Wong, S. T. Lin, J. P. Chang, J. H. Chen, Q. H. Chen, Y. H. Chen, Z. Deng, Q. Du, H. Gong, X. Q. Hao, H. J. He, Q. J. He, H. X. Huang, T. R. Huang, H. Jiang, H. B. Li, J. Li, J. Li, J. M. Li, X. Li, X. Y. Li, Y. L. Li, F. K. Lin, S. K. Liu, L. C. Lü, H. Ma, J. L. Ma, S. J. Mao, J. Q. Qin, J. Ren, J. Ren, X. C. Ruan, V. Sharma, M. B. Shen, L. Singh, M. K. Singh, A. K. Soma, J. Su, C. J. Tang,

-
- J. M. Wang, L. Wang, Q. Wang, S. Y. Wu, Y. C. Wu, Z. Z. Xianyu, R. Q. Xiao, H. Y. Xing, F. Z. Xu, Y. Xu, X. J. Xu, T. Xue, L. T. Yang, S. W. Yang, N. Yi, C. X. Yu, H. Yu, X. Z. Yu, M. Zeng, X. H. Zeng, Z. Zeng, L. Zhang, Y. H. Zhang, M. G. Zhao, Z. Y. Zhou, J. J. Zhu, W. B. Zhu, X. Z. Zhu, and Z. H. Zhu, “Search of low-mass wimps with a p -type point contact germanium detector in the cdex-1 experiment,” *Phys. Rev. D*, vol. 93, p. 092003, May 2016. [Online]. Available: <https://link.aps.org/doi/10.1103/PhysRevD.93.092003>
- [50] A. Aguilar-Arevalo, D. Amidei, X. Bertou, M. Butner, G. Cancelo, A. Castañeda Vázquez, B. A. Cervantes Vergara, A. E. Chavarria, C. R. Chavez, J. R. T. de Mello Neto, J. C. D’Olivo, J. Estrada, G. Fernandez Moroni, R. Gañor, Y. Guardincerri, K. P. Hernández Torres, F. Izraelevitch, A. Kavner, B. Kilminster, I. Lawson, A. Letessier-Selvon, J. Liao, V. B. B. Mello, J. Molina, J. R. Peña, P. Privitera, K. Ramanathan, Y. Sarkis, T. Schwarz, C. Sengul, M. Settimo, M. Sofo Haro, R. Thomas, J. Tiffenberg, E. Tiouchichine, D. Torres Machado, F. Trillaud, X. You, and J. Zhou, “Search for low-mass wimps in a 0.6 kg day exposure of the damic experiment at snolab,” *Phys. Rev. D*, vol. 94, p. 082006, Oct 2016. [Online]. Available: <https://link.aps.org/doi/10.1103/PhysRevD.94.082006>
- [51] A. Tan, M. Xiao, X. Cui, X. Chen, Y. Chen, D. Fang, C. Fu, K. Giboni, F. Giuliani, H. Gong, X. Guo, K. Han, S. Hu, X. Huang, X. Ji, Y. Ju, S. Lei, S. Li, X. Li, X. Li, H. Liang, Q. Lin, H. Liu, J. Liu, W. Lorenzon, Y. Ma, Y. Mao, K. Ni, X. Ren, M. Schubnell, M. Shen, F. Shi, H. Wang, J. Wang, M. Wang, Q. Wang, S. Wang, X. Wang, Z. Wang, S. Wu, X. Xiao, P. Xie, B. Yan, Y. Yang, J. Yue, X. Zeng, H. Zhang, H. Zhang, H. Zhang, T. Zhang, L. Zhao, J. Zhou, N. Zhou, and X. Zhou, “Dark matter results from first 98.7 days of data from the pandax-ii experiment,” *Phys. Rev. Lett.*, vol. 117, p. 121303, Sep 2016. [Online]. Available: <https://link.aps.org/doi/10.1103/PhysRevLett.117.121303>
- [52] L. Hehn, E. Armengaud, Q. Arnaud, C. Augier, A. Benoît, L. Bergé, J. Billard, J. Blümer, T. de Boissière, A. Broniatowski, P. Camus, A. Cazes, M. Chapellier, F. Charlieux, M. De Jésus, L. Dumoulin, K. Eitel, N. Foerster, J. Gascon, A. Giuliani, M. Gros, G. Heuermann, Y. Jin, A. Juillard, C. Kéfélian, M. Kleifges, V. Kozlov, H. Kraus, V. A. Kudryavtsev, H. Le-Sueur, S. Marnieros, X.-F. Navick, C. Nones, E. Olivieri, P. Pari, B. Paul, M.-C. Piro, D. Poda, E. Queguiner, S. Rozov, V. Sanglard, B. Schmidt, S. Scorza, B. Siebenborn, D. Tcherniakhovski, L. Vagneron, M. Weber, and E. Yakushev, “Improved edelweiss-iii sensitivity for low-mass wimps using a profile likelihood approach,” *The European Physical Journal C*, vol. 76, no. 10, p. 548, Oct 2016. [Online]. Available: <https://doi.org/10.1140/epjc/s10052-016-4388-y>
- [53] C. Amole, M. Ardid, I. J. Arnquist, D. M. Asner, D. Baxter, E. Behnke, P. Bhattacharjee, H. Borsodi, M. Bou-Cabo, P. Champion, G. Cao, C. J. Chen, U. Chowdhury, K. Clark, J. I. Collar, P. S. Cooper, M. Crisler, G. Crowder, C. E. Dahl, M. Das, S. Fallows, J. Farine, I. Felis, R. Filgas, F. Girard, G. Giroux, J. Hall, O. Harris, E. W. Hoppe, M. Jin, C. B. Krauss, M. Laurin, I. Lawson, A. Leblanc, I. Levine, W. H. Lippincott,

-
- F. Mamedov, D. Maurya, P. Mitra, T. Nania, R. Neilson, A. J. Noble, S. Olson, A. Ortega, A. Plante, R. Podvianuk, S. Priya, A. E. Robinson, A. Roeder, R. Rucinski, O. Scallon, S. Seth, A. Sonnenschein, N. Starinski, I. Štekl, F. Tardif, E. Vázquez-Jáuregui, J. Wells, U. Wichoski, Y. Yan, V. Zacek, and J. Zhang, “Dark matter search results from the PICO–60 c_3f_8 bubble chamber,” *Phys. Rev. Lett.*, vol. 118, p. 251301, Jun 2017. [Online]. Available: <https://link.aps.org/doi/10.1103/PhysRevLett.118.251301>
- [54] E. Aprile, J. Aalbers, F. Agostini, M. Alfonsi, F. D. Amaro, M. Anthony, F. Arneodo, P. Barrow, L. Baudis, B. Bauermeister, M. L. Benabderrahmane, T. Berger, P. A. Breur, A. Brown, A. Brown, E. Brown, S. Bruenner, G. Bruno, R. Budnik, L. Bütikofer, J. Calvén, J. M. R. Cardoso, M. Cervantes, D. Cichon, D. Coderre, A. P. Colijn, J. Conrad, J. P. Cussonneau, M. P. Decowski, P. de Perio, P. Di Gangi, A. Di Giovanni, S. Diglio, G. Eurin, J. Fei, A. D. Ferella, A. Fieguth, W. Fulgione, A. Gallo Rosso, M. Galloway, F. Gao, M. Garbini, R. Gardner, C. Geis, L. W. Goetzke, L. Grandi, Z. Greene, C. Grignon, C. Hasterok, E. Hogenbirk, J. Howlett, R. Itay, B. Kaminsky, S. Kazama, G. Kessler, A. Kish, H. Landsman, R. F. Lang, D. Lellouch, L. Levinson, Q. Lin, S. Lindemann, M. Lindner, F. Lombardi, J. A. M. Lopes, A. Manfredini, I. Mariş, T. Marrodán Undagoitia, J. Masbou, F. V. Massoli, D. Masson, D. Mayani, M. Messina, K. Micheneau, A. Molinario, K. Morà, M. Murra, J. Naganoma, K. Ni, U. Oberlack, P. Pakarha, B. Pelssers, R. Persiani, F. Piastra, J. Pienaar, V. Pizzella, M.-C. Piro, G. Plante, N. Priel, L. Rauch, S. Reichard, C. Reuter, B. Riedel, A. Rizzo, S. Rosendahl, N. Rupp, R. Saldanha, J. M. F. dos Santos, G. Sartorelli, M. Scheibelhut, S. Schindler, J. Schreiner, M. Schumann, L. Scotto Lavina, M. Selvi, P. Shagin, E. Shockley, M. Silva, H. Simgen, M. v. Sivers, A. Stein, S. Thapa, D. Thers, A. Tiseni, G. Trincherio, C. Tunnell, M. Vargas, N. Upole, H. Wang, Z. Wang, Y. Wei, C. Weinheimer, J. Wulf, J. Ye, Y. Zhang, and T. Zhu, “First dark matter search results from the xenon1t experiment,” *Phys. Rev. Lett.*, vol. 119, p. 181301, Oct 2017. [Online]. Available: <https://link.aps.org/doi/10.1103/PhysRevLett.119.181301>
- [55] D. S. Akerib, S. Alsum, H. M. Araújo, X. Bai, A. J. Bailey, J. Balajthy, P. Beltrame, E. P. Bernard, A. Bernstein, T. P. Biesiadzinski, E. M. Boulton, R. Bramante, P. Brás, D. Byram, S. B. Cahn, M. C. Carmona-Benitez, C. Chan, A. A. Chiller, C. Chiller, A. Currie, J. E. Cutter, T. J. R. Davison, A. Dobi, J. E. Y. Dobson, E. Druszkiewicz, B. N. Edwards, C. H. Faham, S. Fiorucci, R. J. Gaitskell, V. M. Gehman, C. Ghag, K. R. Gibson, M. G. D. Gilchriese, C. R. Hall, M. Hanhardt, S. J. Haselschwardt, S. A. Hertel, D. P. Hogan, M. Horn, D. Q. Huang, C. M. Ignarra, M. Ihm, R. G. Jacobsen, W. Ji, K. Kamdin, K. Kazkaz, D. Khaitan, R. Knoche, N. A. Larsen, C. Lee, B. G. Lenardo, K. T. Lesko, A. Lindote, M. I. Lopes, A. Manalaysay, R. L. Mannino, M. F. Marzioni, D. N. McKinsey, D.-M. Mei, J. Mock, M. Moongweluwan, J. A. Morad, A. S. J. Murphy, C. Nehrkorn, H. N. Nelson, F. Neves, K. O’Sullivan, K. C. Oliver-Mallory, K. J. Palladino, E. K. Pease, P. Phelps, L. Reichhart, C. Rhyne, S. Shaw, T. A. Shutt, C. Silva, M. Solmaz, V. N. Solovov, P. Sorensen, S. Stephenson, T. J. Sumner, M. Szydagis, D. J. Taylor, W. C. Taylor, B. P.

-
- Tennyson, P. A. Terman, D. R. Tiedt, W. H. To, M. Tripathi, L. Tvrznikova, S. Uvarov, J. R. Verbus, R. C. Webb, J. T. White, T. J. Whitis, M. S. Witherell, F. L. H. Wolfs, J. Xu, K. Yazdani, S. K. Young, and C. Zhang, “Results from a search for dark matter in the complete lux exposure,” *Phys. Rev. Lett.*, vol. 118, p. 021303, Jan 2017. [Online]. Available: <https://link.aps.org/doi/10.1103/PhysRevLett.118.021303>
- [56] H. Jiang, L. P. Jia, Q. Yue, K. J. Kang, J. P. Cheng, Y. J. Li, H. T. Wong, M. Agartioglu, H. P. An, J. P. Chang, J. H. Chen, Y. H. Chen, Z. Deng, Q. Du, H. Gong, L. He, J. W. Hu, Q. D. Hu, H. X. Huang, H. B. Li, H. Li, J. M. Li, J. Li, X. Li, X. Q. Li, Y. L. Li, B. Liao, F. K. Lin, S. T. Lin, S. K. Liu, Y. D. Liu, Y. Y. Liu, Z. Z. Liu, H. Ma, J. L. Ma, H. Pan, J. Ren, X. C. Ruan, B. Sevda, V. Sharma, M. B. Shen, L. Singh, M. K. Singh, T. X. Sun, C. J. Tang, W. Y. Tang, Y. Tian, G. F. Wang, J. M. Wang, L. Wang, Q. Wang, Y. Wang, S. Y. Wu, Y. C. Wu, H. Y. Xing, Y. Xu, T. Xue, L. T. Yang, S. W. Yang, N. Yi, C. X. Yu, H. J. Yu, J. F. Yue, X. H. Zeng, M. Zeng, Z. Zeng, F. S. Zhang, Y. H. Zhang, M. G. Zhao, J. F. Zhou, Z. Y. Zhou, J. J. Zhu, and Z. H. Zhu, “Limits on light weakly interacting massive particles from the first 102.8 kg \times day data of the cdex-10 experiment,” *Phys. Rev. Lett.*, vol. 120, p. 241301, Jun 2018. [Online]. Available: <https://link.aps.org/doi/10.1103/PhysRevLett.120.241301>
- [57] Q. Arnaud, D. Asner, J.-P. Bard, A. Brossard, B. Cai, M. Chapellier, M. Clark, E. Corcoran, T. Dandl, A. Dastgheibi-Fard, K. Dering, P. D. Stefano, D. Durnford, G. Gerbier, I. Giomataris, P. Gorel, M. Gros, O. Guillaudin, E. Hoppe, A. Kamaha, I. Katsioulas, D. Kelly, R. Martin, J. McDonald, J.-F. Muraz, J.-P. Mols, X.-F. Navick, T. Papaevangelou, F. Piquemal, S. Roth, D. Santos, I. Savvidis, A. Ulrich, F. V. de Sola Fernandez, and D. m. D. d. L.-m. W. M. Zampaolo, keywords = "Spherical proportional counter, “First results from the news-g direct dark matter search experiment at the lsm,” *Astroparticle Physics*, vol. 97, pp. 54 – 62, 2018. [Online]. Available: <http://www.sciencedirect.com/science/article/pii/S0927650517301871>
- [58] E. Behnke, M. Besnier, P. Bhattacharjee, X. Dai, M. Das, A. Davour, F. Debris, N. Dhungana, J. Farine, M. Fines-Neuschild, S. Gagnebin, G. Giroux, E. Grace, C. Jackson, A. Kamaha, C. Krauss, M. LafreniÃfÃ”re, M. Laurin, I. Lawson, L. Lessard, I. Levine, D. Marlisov, J.-P. Martin, P. Mitra, A. Noble, A. Plante, R. Podviyanuk, S. Pospisil, O. Scallon, S. Seth, N. Starinski, I. Stekl, U. Wichoski, and V. Zacek, “Final results of the picasso dark matter search experiment,” *Astroparticle Physics*, vol. 90, pp. 85 – 92, 2017. [Online]. Available: <http://www.sciencedirect.com/science/article/pii/S092765051730066X>
- [59] “Low-mass dark matter search with cdmslite.” [Online]. Available: <https://arxiv.org/abs/1707.01632v2>
- [60] “First results on low-mass dark matter from the cressst-iii experiment.” [Online]. Available: <https://arxiv.org/abs/1711.07692v1>

-
- [61] R. Agnese, A. J. Anderson, T. Aralis, T. Aramaki, I. J. Arnquist, W. Baker, D. Balakishiyeva, D. Barker, R. Basu Thakur, D. A. Bauer, T. Binder, M. A. Bowles, P. L. Brink, R. Bunker, B. Cabrera, D. O. Caldwell, R. Calkins, C. Cartaro, D. G. Cerdeño, Y. Chang, H. Chagani, Y. Chen, J. Cooley, B. Cornell, P. Cushman, M. Daal, P. C. F. Di Stefano, T. Doughty, L. Esteban, E. Fascione, E. Figueroa-Feliciano, M. Fritts, G. Gerbier, M. Ghaith, G. L. Godfrey, S. R. Golwala, J. Hall, H. R. Harris, Z. Hong, E. W. Hoppe, L. Hsu, M. E. Huber, V. Iyer, D. Jardin, A. Jastram, C. Jena, M. H. Kelsey, A. Kennedy, A. Kubik, N. A. Kurinsky, A. Leder, B. Loer, E. Lopez Asamar, P. Lukens, D. MacDonell, R. Mahapatra, V. Mandic, N. Mast, E. H. Miller, N. Mirabolfathi, R. A. Moffatt, B. Mohanty, J. D. Morales Mendoza, J. Nelson, J. L. Orrell, S. M. Oser, K. Page, W. A. Page, R. Partridge, M. Pepin, M. Peñalver Martinez, A. Phipps, S. Poudel, M. Pyle, H. Qiu, W. Rau, P. Redl, A. Reisetter, T. Reynolds, A. Roberts, A. E. Robinson, H. E. Rogers, T. Saab, B. Sadoulet, J. Sander, K. Schneck, R. W. Schnee, S. Scorza, K. Senapati, B. Serfass, D. Speller, M. Stein, J. Street, H. A. Tanaka, D. Toback, R. Underwood, A. N. Villano, B. von Krosigk, B. Welliver, J. S. Wilson, M. J. Wilson, D. H. Wright, S. Yellin, J. J. Yen, B. A. Young, X. Zhang, and X. Zhao, “Low-mass dark matter search with cdmslite,” *Phys. Rev. D*, vol. 97, p. 022002, Jan 2018. [Online]. Available: <https://link.aps.org/doi/10.1103/PhysRevD.97.022002>
- [62] R. Agnese, Z. Ahmed, A. J. Anderson, S. Arrenberg, D. Balakishiyeva, R. Basu Thakur, D. A. Bauer, J. Billard, A. Borgland, D. Brandt, P. L. Brink, T. Bruch, R. Bunker, B. Cabrera, D. O. Caldwell, D. G. Cerdeno, H. Chagani, J. Cooley, B. Cornell, C. H. Crewdson, P. Cushman, M. Daal, F. Dejongh, E. do Couto e Silva, T. Doughty, L. Esteban, S. Fallows, E. Figueroa-Feliciano, J. Filippini, J. Fox, M. Fritts, G. L. Godfrey, S. R. Golwala, J. Hall, R. H. Harris, S. A. Hertel, T. Hofer, D. Holmgren, L. Hsu, M. E. Huber, A. Jastram, O. Kamaev, B. Kara, M. H. Kelsey, A. Kennedy, P. Kim, M. Kiveni, K. Koch, M. Kos, S. W. Leman, B. Loer, E. Lopez Asamar, R. Mahapatra, V. Mandic, C. Martinez, K. A. McCarthy, N. Mirabolfathi, R. A. Moffatt, D. C. Moore, P. Nadeau, R. H. Nelson, K. Page, R. Partridge, M. Pepin, A. Phipps, K. Prasad, M. Pyle, H. Qiu, W. Rau, P. Redl, A. Reisetter, Y. Ricci, T. Saab, B. Sadoulet, J. Sander, K. Schneck, R. W. Schnee, S. Scorza, B. Serfass, B. Shank, D. Speller, K. M. Sundqvist, A. N. Villano, B. Welliver, D. H. Wright, S. Yellin, J. J. Yen, J. Yoo, B. A. Young, and J. Zhang, “Silicon detector dark matter results from the final exposure of cdms ii,” *Phys. Rev. Lett.*, vol. 111, p. 251301, Dec 2013. [Online]. Available: <https://link.aps.org/doi/10.1103/PhysRevLett.111.251301>
- [63] C. E. Aalseth, P. S. Barbeau, J. Colaresi, J. I. Collar, J. Diaz Leon, J. E. Fast, N. E. Fields, T. W. Hossbach, A. Knecht, M. S. Kos, M. G. Marino, H. S. Miley, M. L. Miller, J. L. Orrell, and K. M. Yocum, “Cogent: A search for low-mass dark matter using p -type point contact germanium detectors,” *Phys. Rev. D*, vol. 88, p. 012002, Jul 2013. [Online]. Available: <https://link.aps.org/doi/10.1103/PhysRevD.88.012002>
- [64] G. Angloher, M. Bauer, I. Bavykina, A. Bento, C. Bucci, C. Ciemniak, G. Deuter, F. von

-
- Feilitzsch, D. Hauff, P. Huff, C. Isaila, J. Jochum, M. Kiefer, M. Kimmerle, J.-C. Lanfranchi, F. Petricca, S. Pfister, W. Potzel, F. Pröbst, F. Reindl, S. Roth, K. Rottler, C. Sailer, K. Schäffner, J. Schmaler, S. Scholl, W. Seidel, M. v. Sivers, L. Stodolsky, C. Strandhagen, R. Strauß, A. Tanzke, I. Usherov, S. Wawoczny, M. Willers, and A. Zöller, “Results from 730 kg days of the cresst-ii dark matter search,” *The European Physical Journal C*, vol. 72, no. 4, p. 1971, Apr 2012. [Online]. Available: <https://doi.org/10.1140/epjc/s10052-012-1971-8>
- [65] “Compatibility of dama/libra dark matter detection with other searches.” [Online]. Available: <https://arxiv.org/abs/0808.3607>
- [66] F. Ruppin, J. Billard, E. Figueroa-Feliciano, and L. Strigari, “Complementarity of dark matter detectors in light of the neutrino background,” *Phys. Rev. D*, vol. 90, p. 083510, Oct 2014. [Online]. Available: <https://link.aps.org/doi/10.1103/PhysRevD.90.083510>